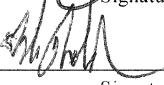**Richard P Fiorella**

Dehumidification Over Tropical Continents Reduces Climate Sensitivity and Inhibits Snowball Earth Initiation

Submitted for Publication in:

Journal of Climate

in lieu of thesis in partial fulfillment of the requirements for the degree of
Master of Science in Earth and Environmental Sciences
Department of Earth and Environmental Sciences
The University of Michigan

Accepted by:

_____ Signature	*Chris J. Poulsen*	11/14/12
	Name	Date
_____ Signature	Nathan D. Sheldon	30 November 2012
	Name	Date
Rebecca Lange _____ Department Chair Signature	Rebecca Lange	12/11/2012
	Name	Date

I hereby grant the University of Michigan, its heirs and assigns, the non-exclusive right to reproduce and distribute single copies of my thesis, in whole or in part, in any format. I represent and warrant to the University of Michigan that the thesis is an original work, does not infringe or violate any rights of others, and that I make these grants as the sole owner of the rights to my thesis. I understand that I will not receive royalties for any reproduction of this thesis.

☐ Permission granted.

☒ Permission granted to copy after: 7/1/2013

☐ Permission declined.

Author Signature

Earth and Environmental Sciences
UNIVERSITY OF MICHIGAN

1 **Dehumidification over Tropical Continents Reduces Climate Sensitivity and Inhibits**

2 **Snowball Earth Initiation**

3 Richard P Fiorella[1] and Christopher J Poulsen[1]

4 1: Department of Earth and Environmental Sciences, University of Michigan, Ann Arbor, MI

5 48109

6 *Corresponding author address:* Richard P. Fiorella, Department of Earth and Environmental

7 Sciences, University of Michigan, 2534 CC Little Building, 1100 N. University Avenue, Ann

8 Arbor, MI 48109-1005, USA

9 *Email:* richf@umich.edu

10

11

12

13

14

15

16

17

18

19

20

21

22

23

24 **Abstract**

25 The enigmatic Neoproterozoic geological record suggests the potential for a fully glaciated

26 "Snowball Earth." Low-latitude continental position has been invoked as a potential Snowball

27 Earth trigger by raising surface albedo and reducing atmospheric CO_2 concentrations through

28 increased silicate weathering. Herein, climate response to reduction of total solar irradiance (TSI)

29 is tested using four different land configurations (aquaplanet, modern, Neoproterozoic, and low-

30 latitude supercontinent) with uniform topography in the NCAR Community Atmosphere Model

31 (CAM, version 3.1) general circulation model with a mixed-layer ocean. Despite a lower surface

32 albedo at 100% TSI, the threshold for global glaciation decreases from 92% TSI in the

33 aquaplanet configuration to 85% TSI with a low-latitude supercontinent. The difference in

34 thresholds is principally due to the sensitivity of total specific humidity and therefore greenhouse

35 forcing to reductions in TSI. Dehumidification of the troposphere over large tropical continents

36 decreases greenhouse forcing and also increases direct heating by decreasing cloud cover.

37 Continental heating intensifies the Walker circulation and the transport of dry air over the ocean,

38 enhancing surface evaporation and marine tropospheric humidification, maintaining a high

39 specific humidity and greenhouse effect over the ocean. Topography also provides an important

40 control on Snowball Earth initiation. Modern topography in the modern continental arrangement

41 lowers the initiation threshold by up to 2% TSI relative to a modern continental arrangement

42 without topography. In the absence of potential silicate weathering feedbacks, large tropical

43 landmasses raise the barrier to initiation of Snowball events. More generally, these simulations

44 demonstrate the substantial influence of geography on climate sensitivity.

45

46

2

1. Introduction

Several lines of geologic evidence from the mid and late Neoproterozoic suggest the episodic occurrence of prolonged low-latitude glaciation and perhaps a "Snowball Earth" resulting from global glaciation. Cryogenian (850-630 Ma) glaciogenic sequences and diamictites are found on every continent and are frequently overlain by thick "cap" carbonate sequences. Large and chemostratographically correlated carbon isotope anomalies in these cap carbonates are thought to reflect the global nature of mid and late Neoproterozoic glaciations (Hoffman and Schrag 2002; Macdonald et al. 2010). Iridium anomalies found at the base of cap carbonates in Africa suggest that the Marinoan glaciation episode lasted at least 3 million years, but more likely 12 million years (Bodiselitsch et al. 2005), though these results have not been duplicated in other cap carbonate sequences. Finally, the return of banded iron formations in the Neoproterozoic after a billion year hiatus (Hoffman and Schrag 2002; Pierrehumbert et al. 2011) has been argued to be evidence of ocean anoxia during the glaciation event, though the chemical conditions facilitating their deposition in the Neoproterozoic were likely different and more directly dependent on ocean composition than during the Paleoproterozoic. Deep ocean anoxia during Neoproterozoic glaciations may have been brought about by tropical pack ice interfering with and weakening wind-driven ocean circulation or total isolation of the ocean from the atmosphere by sea ice (Kirschvink 1992). Termination of Snowball Earth is thought to have resulted from buildup of atmospheric CO_2 levels over millions of years as silicate weathering essentially stopped during the Snowball event while volcanic outgassing would have continued unabated. Supporting this suggestion, strongly negative $\Delta^{17}O$ anomalies in Neoproterozoic sulfate minerals precipitated after termination of Snowball events suggest higher CO_2 levels than at any point during the Phanerozoic (Bao et al. 2008; 2009).

70   However, not all geologic evidence is compatible with Snowball Earth. Biomarker

71   evidence of eukaryotic life dates back to the Archean (Waldbauer et al. 2009) while evidence of

72   sponges exists prior to the Marinoan glaciation (Love et al. 2008). Therefore, emergence of

73   Metazoan life predated the Snowball events and Metazoan survival calls into question likely

74   global temperatures during the existence of a completely glaciated ocean. Additionally, while

75   deposition of cap carbonates is thought to reflect amplified continental weathering or overturning

76   of a stratified ocean following deglaciation (Hoffman and Schrag 2002), critics have questioned

77   how these mechanisms could produce widespread and synchronous carbonate deposition

78   (Ridgwell et al. 2003; Shields 2005).

79   Efforts using climate models to understand Neoproterozoic climate have only stoked the

80   Snowball debate. According to standard solar evolution models, solar luminosity during the

81   Neoproterozoic would have been approximately 6-7% lower than present (Gough 1981; Crowley

82   and Baum 1993). Energy balance models (EBM) developed independently by Budyko (1969)

83   and Sellers (1969) suggest global glaciation driven by a runaway ice-albedo feedback could

84   result from modest reductions in solar luminosity (as little as 1.6%) after ice expands

85   equatorward beyond a critical latitude. Improvements to EBM parameterization of heat transport

86   and thermal diffusion made by North (1975a,b) suggested global glaciation might occur with

87   reductions in solar luminosity closer to 7%.

88   Snowball Earth initiation has also been explored in several general circulation models

89   (GCMs). Larger reductions of total solar irradiance (TSI) are typically required in GCMs to

90   simulate a Snowball state than in EBMs, suggesting that climate dynamics and feedbacks not

91   captured in EBMs restrict ice expansion. In support of this conclusion, previous studies have

92   identified processes including ocean heat transport (Poulsen et al. 2001; Bendtsen 2002), wind-

93   driven ocean circulation, and cloud-radiative forcing (Poulsen and Jacob 2004) that restrict sea-

94   ice growth. For example, clouds over sea-ice restrict surface sensible heat loss and have a

95   warming effect over sea-ice. The ice-albedo feedback is weaker than when cloud radiative

96   forcing is excluded (Poulsen and Jacob 2004). Likewise, ocean circulation transports heat to and

97   stabilizes the ice line. Convective mixing warms the surface ocean adjacent to the ice margin

98   restricting ice growth, with the largest impact occurring in the winter (Poulsen et al. 2001).

99   Nonetheless, a wide range of solar luminosity thresholds for Snowball initiations have

100   been reported (Pierrehumbert et al. 2011). With Marinoan continents, the ECHAM/MPI-OM

101   model predicts a Snowball state when solar luminosity is reduced below 96% of the modern

102   value (Voigt et al. 2011). With comparable greenhouse gas concentrations, however, other

103   models including FOAM (e.g., Poulsen et al. 2001; Poulsen 2003), GISS (e.g., Chandler and

104   Sohl 2000), and GENESIS (e.g., Baum and Crowley 2001; 2003) fail to simulate Snowball states

105   when solar luminosity is reduced below 94%. Other solutions in addition to global ice cover have

106   also been invoked to explain the geologic evidence. "Slushball" or "waterbelt" solutions (e.g.,

107   Hyde et al. 2000; Chandler and Sohl 2000; Baum and Crowley 2001; 2003; Micheels and

108   Montenari 2008) describe a state with glaciated continents but ice-free tropical oceans and ice

109   margins poleward of 25° latitude. In these studies, however, a large portion of land was

110   positioned in mid and high latitudes, at odds with paleogeographic reconstructions for the

111   Marinoan and Sturtian glaciations (Hoffman and Li 2009). An additional solution, the

112   "Jormungand" state—named for the serpent-like appearance of a narrow band of iceless

113   equatorial ocean in a Hovmöller diagram—emerges when the albedo of snow-covered and bare

114   sea-ice differ (Abbot et al. 2011). These open-ocean solutions provide an attractive explanation

115   for glaciogenic deposits in low paleolatitudes and provide a refuge for life, but may fail to

116   account for the deposition of banded iron formations since the wind-driven ocean circulation

117   would likely prevent the deep oceans from becoming anoxic.

118   Across these models, a myriad of paleogeographies has been used and may in part be

119   responsible for the range of observed sensitivities. Here, we investigate the hypothesis that low

120   latitude continents facilitate Snowball Earth initiation (Kirschvink 1992). Multiproxy

121   reconstructions of Neoproterozoic geography place the bulk of the land area in the tropics and

122   the subtropics (Kirschvink 1992; Li et al. 2008; Hoffman and Li 2009), a distribution that has

123   been considered conducive to Snowball Earth initiation for three major reasons. First, land

124   surfaces generally have higher albedo than ocean, particularly under the relatively cloud-free

125   descending limb of the Hadley cell in the subtropics where surface albedo has a stronger impact

126   on planetary albedo. Second, as continental glaciers form and sea-level drops, land would replace

127   shallow seas in the tropics, further increasing albedo (Kirschvink 1992). Finally, weathering

128   rates of silicate minerals would increase with increased land under the intertropical convergence

129   zone, leading to an enhanced drawdown of atmospheric CO_2 under a constant volcanic degassing

130   rate (Marshall et al. 1988; Worsley and Kidder 1991).

131   Previous studies provide conflicting conclusions about the impact of increased tropical

132   landmass on global average temperatures. GCM experiments generally suggest higher global

133   temperatures when more land is concentrated in the tropics. For example, Barron et al. (1984)

134   show tropical continents suppress evaporative cooling and warm the tropics and Poulsen et al.

135   (2002) suggest mid and high-latitude continents promote cooling by increasing snow coverage

136   over continents and sensible heat loss from the ocean, leading to greater global ice coverage. In

137   contrast, Voigt et al. (2011) argue that increased tropical landmass cools global temperatures by

138   increasing planetary albedo and weakening the greenhouse effect. Here, we analyze how climate

139 sensitivity to reduction in solar luminosity varies with paleogeography and describe its

140 implications for snowball Earth initiation.

141

142 **2. Model Description and Setup**

143 Snowball Earth initiation experiments were performed using the National Center for

144 Atmospheric Research Community Atmosphere Model (CAM) version 3.1 (Collins et al. 2004),

145 consisting of an atmospheric model coupled to a 50-m mixed-layer ocean model and the

146 Common Land Model (CLM) version 3.0 (Oleson et al. 2004). A horizontal resolution of

147 spectral T31 (~3.75°) was used in the atmospheric model, with 26 levels in the vertical using a

148 terrain-following vertical coordinate (Collins et al. 2004). The model top is in the stratosphere at

149 3.5 hPa, and model levels are roughly split equally between the troposphere and stratosphere. No

150 additional heat transport was specified for the mixed-layer ocean, and dynamic adjustments to

151 the mixed-layer ocean heat flux were disabled. Sea-ice is modeled purely on a thermodynamic

152 basis with no dynamics included. To generate a better match with modern sea ice distributions,

153 the mixed-layer ocean model in CAM adds 15 W m^{-2} to the Northern Hemisphere ocean and

154 removes 10 W m^{-2} from the Southern Hemisphere ocean by default; these values were set to zero

155 everywhere in our experiments.

156 Neoproterozoic boundary conditions are not well constrained. Model boundary

157 conditions were chosen to best represent the Neoproterozoic, to facilitate glaciation, and to

158 simplify analysis of results. Eccentricity was set to zero and obliquity was held constant at 23.5°.

159 Carbon dioxide (280 ppm), aerosol, and ozone concentrations were set to preindustrial levels.

160 Model default values were used for methane (1714 ppb) and nitrous oxide (316 ppb); sensitivity

161 tests indicate this choice does not fundamentally alter the results presented here. As land plants

162   had not evolved in the Neoproterozoic, all land vegetation was removed and the land surface

163   specified as desert. CLM calculates the land surface albedo as a function of soil color and the

164   moisture content of the topsoil layer. The lightest, most reflective soil color is used, having

165   visible/near-infrared (NIR) albedos of 0.24/0.48 when the top layer of soil is dry, and decreasing

166   to 0.12/0.24 when the top soil layer is saturated (Oleson et al. 2004). Ocean albedo is 0.06 for

167   direct sunlight in these experiments. The albedo of sea ice increases linearly with thickness up to

168   1 m, at which albedos are capped at 0.67 in the visible and 0.30 for NIR wavelengths. Cold snow

169   has an albedo of 0.91/0.63 for visible/NIR wavelengths.

170   We test four different continental arrangements: (a) an aquaplanet with no land (hereafter

171   AQP), (b) an equator-centered rectangular supercontinent extending to 43°N/S and spanning

172   130° degrees in longitude (hereafter RECT), (c) a continental reconstruction with two large

173   tropical continents (hereafter MAR), based on the Marinoan (~635 Ma) paleogeography used in

174   Voigt et al. (2011), and (d) a modern continental configuration with topography removed

175   (hereafter MOD-NT) (see Fig. 1 for configurations). A summary of all of the runs performed is

176   provided in Table 1. Global land fraction was similar across the configurations with 32.3%,

177   27.8% and 27.0% land coverage for the MOD-NT, MAR, and RECT experiments respectively

178   (Table 2). Low-latitude (≤30°) land fraction is 28.8%, 48.1% and 38.5% for the MOD-NT, MAR,

179   and RECT experiments. Land surface elevations are 100 m in all experiments.

180   For the RECT, MAR, and MOD-NT configurations, atmospheric temperatures were

181   initialized with a cosine latitudinal gradient ranging from 28°C at the equator to 12°C at the

182   poles, and initial wind conditions were calculated using the thermal wind. Sea-surface

183   temperatures were prescribed using results from a coupled CCSM run simulating modern climate.

184   The model was run at 100% of the modern solar constant for 100 years, after which branch runs

185   were performed by immediately reducing TSI to values as low as 80% (Table 1). A 1% reduction

186   in TSI corresponds to a global average change in incoming solar radiation at the top of the

187   atmosphere of 3.4 W m^{-2}. As stable climate states lacking permanent sea ice have been reported

188   for modern TSI (e.g., Pierrehumbert et al. 2011), additional sensitivity experiments were

189   performed with no initial ice and initial atmosphere and ocean temperatures set to 300K

190   everywhere. Results presented here were insensitive to this change in initial boundary conditions.

191   In all cases, the model was run until the surface temperature trend over a twenty year

192   period was less than 1°C per century, signifying a quasi-equilibrium state was reached. To

193   ensure these equilibria are stable, we integrated several simulations for additional time,

194   particularly near the bifurcation points (Table 1). Results shown here represent averages of the

195   final 20 years of model integration.

196

197   **3.   Results**

198   *a) Climate sensitivity to TSI*

199   At 100% TSI, mean annual surface temperatures are similar for all four geographies, ranging

200   between 272.4 and 274.0K (Table 2). In all cases, surface temperatures are highly zonal due to

201   the lack of topography, with some asymmetries near the edges of continents (Figs. 1a-d),

202   presumably due to land/sea thermal contrasts. An equator-to-pole temperature gradient of 70K is

203   simulated. Equatorial temperatures average ~295K while polar temperatures average ~225K for

204   all four geographies. Global surface albedo varies from a maximum of 0.356 for the MAR

205   geography to a minimum of 0.310 for the AQP geography due to differing meridional

206   distribution of land. The range in planetary albedo between the geographies at 100% TSI is more

207   than five times smaller than the surface albedo range (0.406 for AQP and 0.397 for MOD-NT),

208   and as a result, surface temperatures only vary by 1.6K. The mean climatological positions of sea

209   ice are also similar for all four geographies, ranging from a maximum equatorward extent of

210   39.7°N/39.3°S (RECT) to a minimum equatorward extent of 42.7°N/40.5°S (MOD-NT).

211   When TSI is reduced to 95%, prominent differences between the AQP and MOD-NT,

212   MAR, and RECT simulations emerge. Despite a surface albedo 13% lower at 100% TSI than the

213   MAR geography, the AQP configuration shows the highest sensitivity to TSI (Figs. 1e-h). AQP

214   equatorial temperatures decrease to 278K and polar temperatures decrease to 190K, yielding an

215   increased equator-to-pole temperature gradient of 88K. In contrast, equatorial and polar

216   temperatures fall to 285-290K and 200-210K for the three geographies with land. As TSI is

217   further reduced, AQP continues to cool most rapidly with TSI, but the MOD-NT, MAR, and

218   RECT climatologies diverge as ice expands equatorward and show a greater range of sensitivity

219   to TSI at lower values (Fig. 2). For example, at 90% TSI the MOD-NT configuration has an

220   average surface temperature 4.3K cooler than the MAR and 7.2K cooler than the RECT

221   simulations. Differing sea-ice cover drives these temperature differences. MOD-NT has the

222   largest ice extent at this TSI (Fig. 2c), particularly in the Southern Hemisphere where there is

223   less land, followed by MAR which has slightly greater ice expansion in the Northern

224   Hemisphere compared to RECT. As a result, planetary albedo increases more in the MOD-NT

225   and MAR cases than in the RECT case.

226   As a result of these varying sensitivities, the threshold TSI for snowball state initiation

227   differs between geographies. Though the configurations with land concentrated in the low-

228   latitudes have slightly higher initial surface albedo at 100% TSI, both surface and planetary

229   albedo for the AQP configuration increases more rapidly with reductions in TSI and is higher at

230   TSI below 100% (Figs. 2c,d). All four configurations exhibit a strong bifurcation point at the

231   transition between partial and global ice coverage. AQP enters the snowball state at the highest

232   solar constant, transitioning to full ice coverage between 92 and 91% TSI. The snowball

233   transitions occur at 88, 86, and 85% of modern TSI for the MOD-NT, MAR, and RECT

234   configurations. Across the AQP, MOD-NT, and MAR experiments, the reduction in TSI

235   necessary to induce a snowball state increases with low-latitude land fraction. Despite having

236   less low-latitude land area than MAR, the RECT configuration experiences global sea-ice cover

237   at a lower TSI, suggesting that continentality also impacts snowball initiation.

238   Geography also impacts the global mean surface temperature at the bifurcation point, as

239   the minimum surface temperature without global ice cover is 233.3K for AQP but 237.2K for

240   RECT. Similarly, the latitude of maximum ice extent before transition to global ice cover for

241   AQP is closer to the equator (10.6°N/9.4°S) than for any of the other configurations. The

242   minimum latitude of stable ice margins for the MOD-NT and MAR experiment are

243   11.8°N/10.0°S and 10.5°N/13.6°S, respectively, while the minimum stable ice margin for the

244   RECT experiments is 12.4°N/10.4°S. In the following sections, we address the energetic and

245   dynamical differences leading to the highly varied responses in TSI reduction and snowball earth

246   initiation to differences in geography.

247

248   *b) Tropical Energy Balance: Cloud and Water Vapor Feedbacks*

249   Low-latitude continents are thought to facilitate global ice cover by reducing absorbed shortwave

250   radiation though increased surface albedo. Our results suggest something different: particularly

251   in the deep tropics, the net shortwave radiation received at the surface is greater for geographies

252   with more tropical land despite a higher surface albedo because of the near absence of clouds

253   over large land masses. Equatorward of 10°, absorbed shortwave radiation is 30 W m^{-2} and 20 W

254 m^{-2} higher for the RECT and MAR geographies than for the AQP geography (Fig. 3a).

255 Longwave radiation shows an even larger disparity between the RECT and AQP geographies,

256 with emission being ~40 W m^{-2} higher in these latitudes in the RECT case (Fig. 3b). Clouds are

257 universally cooling in the tropics at 100% TSI, but the amount of cooling varies by 20-30 W m^{-2}

258 between the geographies, with the AQP and MOD-NT geographies having the most negative

259 cloud forcings (Fig. 3c). This difference in cloud forcing results from stark differences in tropical

260 cloud fraction between the geographies (Fig. 4). Cloud fractions over land, particularly in the

261 subtropics, tend to remain below 0.3 while exceeding 0.6 over the oceans at comparable latitudes.

262 Presence of continents also reduces cloud fractions over the ocean near land (Fig. 3e, 4)

263 increasing cloud radiative forcing over the ocean. This effect is most pronounced in the RECT

264 case, where cloud forcing over the ocean in the deep tropics are 20 W m^{-2} higher than in the AQP

265 case at 100% TSI.

266 Geography alters tropical energy balance, as shown by the large disparities in surface

267 shortwave absorption and longwave emission between cases. The higher sensitivity of AQP to

268 TSI reduction is related to its larger dependence on greenhouse forcing to maintain energy

269 balance (Fig 5). Specific humidity (q) and surface temperature (T) are tightly coupled through

270 the Clausius-Clapeyron equation in all of our simulations (Fig. 6a). Reductions in TSI reduce

271 direct solar heating linearly, while greenhouse forcing decreases nearly exponentially above the

272 bifurcation points for all geographies (Fig 5d). Therefore, TSI reductions have the strongest

273 impact on global temperatures in AQP resulting from its large greenhouse forcing term in the

274 tropical energy balance. In contrast, configurations with land have a larger radiatively direct

275 proportion of the energy budget and therefore show lower sensitivities to TSI reductions than

276 AQP. Among configurations with land, the RECT (MOD-NT) configuration has the largest

12

277   (smallest) radiatively direct energy budget portion (Figs. 3,5), and shows the lowest (highest)

278   sensitivity in q to changes in TSI (Fig. 6b). Tight q-T coupling suggests dynamical differences

279   between the experiments affect energy partitioning that drives the different sensitivities to

280   changes in TSI observed.

281

282   *c) Amplified Walker-like circulation in configurations with high tropical land area*

283   For clarity, we focus on the differences between the AQP and RECT configurations to assess the

284   impact of large land-sea contrasts on zonal circulation patterns in the deep tropics. AQP shows

285   strong upward motion at all longitudes to about 350 mb (Fig. 7). The atmosphere is nearly

286   saturated at the surface and in the upper troposphere. In contrast, RECT shows strong and deeper

287   upward motion over the ocean (to about 250 mb), but strong radiatively driven subsidence in the

288   upper and mid troposphere over the continent, limiting upward motion to the boundary layer and

289   leading to low relative humidity over the continent. Relative humidity drops below 5% over the

290   western third of the continent. Temperatures over the oceans decrease with altitude following

291   the moist adiabatic lapse rate, while dry subsiding air over the continent warms near the dry

292   adiabatic lapse rate during adiabatic descent. As a result of this increased lapse rate as well as

293   increased direct solar heating in the absence of clouds, temperatures at the surface are warmer

294   than they would be were there no continent. Surface winds advect this warm, dry continental air

295   over the oceans, increasing surface evaporation (Fig. 8). Though higher amounts of land decrease

296   the total water flux from tropical oceans, evaporation is more efficient over the ocean in the

297   MAR and RECT cases. Warmer global temperatures and enhanced ocean surface water fluxes

298   yield higher specific humidity over the oceans for the RECT configuration than for the AQP at

299   lower TSIs, particularly in the mid and upper troposphere (Fig. 7) where water vapor has a more

13

300   potent greenhouse effect relative to the boundary layer (Held and Soden 2000). The MAR and

301   MOD-NT configurations also show a Walker cell, but both are weaker than the RECT cell as the

302   amount of contiguous land in the deep tropics is lower and land-sea contrasts are less extreme.

303   Higher moisture contents over the RECT ocean imply the potential for greater latent heat

304   release, driving deeper convection. Convective precipitation rates are double those over the

305   ocean at 95 and 93% TSI in the RECT geography compared to AQP. Deeper convection and

306   increased atmospheric moisture content changes the vertical distribution of clouds (Fig 9) and

307   may be responsible for the increased cloud forcing over the oceans in the RECT case compared

308   to the AQP case. As noted above, clouds are nearly absent over the continent but over the oceans,

309   midlevel cloud cover decreases and high-level cloud cover increases in the tropics and subtropics

310   (Fig. 9). With higher moisture contents, low-level clouds tend to have a stronger impact on

311   shortwave forcing due to higher optical depth while high-level clouds tend to have a stronger

312   warming effect through increased longwave forcing (Hartmann 1994). As a result, the shift in the

313   vertical distribution of clouds results in 20-40 W m^{-2} more shortwave warming in the RECT case

314   while longwave warming is only reduced by 10-15 W m^{-2}, suggesting that the enhanced Walker

315   circulation warms the deep tropics by 5-30 W m^{-2} through altering the cloud distribution.

316

317   *d) Effect of topography in the Modern Simulations*

318   To assess the impact of topography on Snowball initiation, we performed additional simulations

319   using the modern continental arrangement with modern topography (MOD-WT). Including

320   topography lowers the Snowball Earth initiation threshold from 90% in the MOD-WT case to

321   88% in the MOD-NT case. At TSI higher than the bifurcation point, however, mean annual

322 surface temperature and surface and planetary albedo remain similar (Fig. 10), indicating that the

323 change in the bifurcation point cannot be explained by a difference in global albedo.

324   Topography reduces the equator-to-pole temperature gradient by up to 15K, a change that

325 is attributed to increases in subtropical albedo and decreases in midlatitude albedo (particularly

326 in the northern hemisphere), which change the albedo distribution without changing planetary

327 albedo (Fig. 11b). The meridional distribution of albedo changes in response to a decrease

328 (increase) of cloud cover (Fig. 11c) and snow depth (Fig. 11d) in the midlatitudes (subtropics).

329 Though Figure 11 shows results for 90% TSI, the trend shown is present for all TSI above the

330 bifurcation point. The magnitude of this albedo change increases with decreasing TSI, driving an

331 increasingly small equator-to-pole temperature gradient relative to MOD-NT in the MOD-WT

332 simulations as TSI is reduced to the bifurcation points.

333   This redistribution of albedo alters the top of the atmosphere radiative balance, warming

334 the midlatitudes and cooling the subtropics in MOD-NT. Temperatures in the northern

335 hemisphere midlatitudes increase by 15K. Ice expands more rapidly with reduction in TSI with a

336 decreased meridional temperature gradient as a negative global temperature perturbation plunges

337 a larger area below freezing causing greater expansion of sea-ice. This effect is especially

338 apparent as ice encroaches into the tropics where the meridional temperature gradient is weaker

339 than in the subtropics and midlatitudes.

340

341 **4. Discussion**

342 *a) Paleogeographic controls on Snowball Earth initiation*

343 The forcings required to initiate a snowball state for all continental configurations tested here

344 require reductions in TSI below expected Neoproterozoic values based on the standard solar

345 evolution model. Therefore, our results do not directly support the "Hard Snowball" hypothesis,

346 though it is possible radiation receipt at the surface may have been lower through mechanisms

347 other than reduced solar irradiance, such as an increase in volcanic aerosols or a lower

348 concentration of greenhouse gases than used in these simulations. Our results do suggest,

349 however, that if Neoproterozoic glaciations were global, concentration of land in the tropics was

350 unlikely to be the facilitating factor.

351   Land surface albedos in these simulations are lower than those in previous studies. Desert

352 soil albedos (0.35 and 0.51 in the visible and near-infrared) in the FOAM (e.g., Poulsen et al.

353 2001; Poulsen 2003; Poulsen and Jacob 2004) and GENESIS (e.g., Baum and Crowley 2001;

354 2003) models are based on the biosphere-atmosphere transfer scheme (Dickinson et al. 1993).

355 Surface albedos in the GISS model (0.35 in both visible and near-infrared, Hansen et al. 1983)

356 are slightly lower in the near-infrared than the FOAM or GENESIS models. Land albedo may

357 play a strong role in setting the strength of the Walker circulation observed through modulating

358 the intensity of radiatively driven subsidence over the continent as well as the size of the

359 radiatively direct portion of the surface energy budget. Land surface albedos in the

360 Neoproterozoic are poorly constrained, but albedos lower than those in modern deserts might be

361 reasonable as a result of land surface coverage by ancient terrestrial microbial communities

362 (Lenton and Watson 2004; Knauth and Kennedy 2009).

363   The impact of paleogeography on Snowball initiation within one model may be as large

364 as variation between models. For example, Snowball initiation experiments for modern

365 continents with modern topography with CCSM3 (CAM coupled to dynamic ocean and sea-ice

366 models, Collins et al. 2006) by Yang et al. (2012a) yield a Snowball state with a reduction

367 between 10 and 10.5% TSI; our experiments predict a Snowball state with a reduction between

368   10 and 11% TSI. In contrast, larger TSI reduction are required for the RECT geography in CAM

369   than required in FOAM for a similar idealized supercontinent (Poulsen and Jacob 2004). In

370   Poulsen and Jacob (2004), a CO_2 concentration of 140 ppm was used, reducing greenhouse

371   radiative forcing by 3.7 W m^{-2} (Myhre et al. 1998). Assuming a fairly low planetary albedo of

372   0.3 near the bifurcation point, however, the extra 6% reduction in TSI necessary to initiate a

373   Snowball Earth in our experiments represents a 14.4 W m^{-2} change in top of the atmosphere

374   radiative forcing, indicating Snowball states are more difficult to simulate in CAM. Finally,

375   much larger reductions in TSI for Snowball Earth initiation are required herein than for

376   experiments performed in ECHAM5/MPI-OM for both the modern (Voigt and Marotzke 2009)

377   and Marinoan (Voigt et al. 2011) continental configurations.

378   A large portion of the initiation threshold range can be attributed to model differences in

379   albedo parameterizations (Pierrehumbert et al. 2011). Ice albedos in FOAM exceed ice albedos

380   in CAM by ~0.10, suggesting a stronger ice-albedo feedback in FOAM than CAM with all else

381   equal. Supporting this conclusion, setting both FOAM and CAM ice albedos to 0.6 yields

382   identical initiation thresholds (Pierrehumbert et al. 2011). Comparison between ECHAM and

383   CAM is more challenging. Ice albedo in ECHAM (0.75 below -1°C, Roeckner et al. 2003) is

384   similar to the snow covered sea-ice albedo in CAM (broadband albedo ≈0.74 for T31, Collins et

385   al. 2004; Pierrehumbert et al. 2011). CAM tracks snow on sea-ice and assigns a higher albedo to

386   snow covered sea-ice, however, while ECHAM does not. As ice entering in the subtropics is

387   more likely to be bare, model solutions for ECHAM and CAM diverge when ice encroaches on

388   the subtropics (Abbot et al. 2011), therefore, a stronger ice albedo feedback may in part explain

389   the difference between our results in CAM and reported ECHAM/MPI-OM results (Voigt and

390   Marotzke 2009; Voigt et al. 2011). Pierrehumbert et al. (2011) note however, that initiation of

391 snowball states using ECHAM remains easier than using CAM when the snow and sea-ice

392 albedos are all set to 0.6, suggesting differences in atmospheric circulation or cloud forcing

393 between the models must also play a role. Further supporting this conclusion, snowball states

394 remain easier to simulate in ECHAM in the mixed-layer ocean configuration as compared to

395 CAM (Pierrehumbert et al. 2011).

396   Differences in complexity between models used to approach the Snowball problem also

397 certainly play a role in expanding the range of initiation thresholds. The absence of dynamic

398 ocean circulation and sea ice are limitations of our study. Previous studies using both diffusive

399 energy balance models (Rose and Marshall 2009) and general circulation models (Poulsen et al.

400 2001) find that ocean heat transport stabilizes sea-ice margins at higher latitudes. As a result,

401 addition of ocean heat transport to our model would imply increased TSI thresholds for global

402 glaciation. Addition of sea-ice dynamics may limit the stabilizing effect of ocean heat transport,

403 however. Experiments by Yang et al. (2012a) show a rapid transition between a stable state with

404 ~40% sea ice coverage and one with ~60% ice coverage when CO_2 concentration is reduced

405 from 70 to 50 ppm at 94% TSI, a change in radiative forcing of about 1.8 W m^{-2} (Myhre et al.

406 1998). Global ice coverage occurs when CO_2 is further lowered to 17.5 ppm, suggesting this

407 high ice-coverage state is only stable in a small parameter space. Curiously, this rapid transition

408 was not observed when TSI is lowered instead of CO_2. Yang et al. (2012a) attribute this to the

409 latitudinal dependence of solar radiative forcing compared to the latitudinal independence of

410 greenhouse forcing for well-mixed greenhouse gases, using a modified EBM to show that when

411 the ice line expands equatorward of 20°, sensitivity due to solar forcing is stronger than

412 sensitivity due to greenhouse gas forcing.

413   Jormungand states, defined by Abbot et al. (2011) as stable ice latitudes equatorward of

414   25°, were simulated for all four geographies. Unlike the results in Abbot et al. (Abbot et al.

415   2011), we do not find a rapid transition between ice-free conditions and the Jormungand state.

416   Immediate transition between an ice-free state and the Jormungand state is attributed to model

417   deficiencies associated with the idealized configuration of CAM (aquaplanet with no aerosols,

418   modified greenhouse gas concentrations, no ocean heat transport, detailed further in

419   Pierrehumbert et al. 2011). Our choice to vary TSI instead of greenhouse gas concentration may

420   be responsible for the absence of the strong bifurcation between ice-free conditions and the

421   Jormungand state. Radiative forcing was never high enough to simulate an ice-free state in our

422   experiments, but states with stable ice latitudes intermediate to ice-free and Jormungand states

423   likely result from a smaller reduction in radiative forcing in the extratropics from TSI reductions

424   relative to the reduction in radiative forcing resulting from reduced greenhouse gas

425   concentrations. For the same reduction in global radiative forcing, reductions in greenhouse

426   forcing affect all latitudes similarly while the impact of TSI reductions is most pronounced in the

427   tropics due to the latitudinal dependence of solar insolation (Yang et al. 2012a,b).

428   A final attractive aspect of the low-latitude continent Snowball Earth initiation theory

429   was that as glaciers formed on land, sea level would drop exposing continental shelves and

430   further increasing surface albedo as land replaces ocean. Instead, our results suggest as sea level

431   drops and shallow seas in the tropics are replaced by land, Snowball Earth initiation becomes

432   more difficult as continental interiors dry, land-sea contrast becomes more pronounced, and a

433   Walker-style circulation intensifies.

434

435   *b) Paleogeographic impacts on climate sensitivity*

436 The impact of paleogeography on global temperatures remains an open question. On one hand,

437 several studies report higher global temperatures when tropical land area is increased as a result

438 of suppressed precipitation and evaporative cooling in the tropics (Barron et al. 1984). Our

439 results also suggest tropical continents increase global temperatures at decreased TSI, though our

440 simulations don't include the effect of geochemical processes such as silicate weathering.

441 Conversely, simulations with ECHAM/MPI-OM show lower global temperatures when tropical

442 land area is increased (Voigt et al. 2011), and a more facile Snowball Earth initiation. Initiation

443 of a Snowball state using a modern continental arrangement and topography required a 1.5%

444 greater reduction (to 94%) in TSI than initiation of a Snowball state using a Marinoan

445 reconstruction (Voigt and Marotzke 2009). Voigt et al. (2011) relate this difference to elevated

446 albedo and a weakened greenhouse effect when land is shifted equatorward. This comparison is

447 complicated and possibly compromised by inclusion of land plants in the modern simulation,

448 however, which may have promoted a stronger greenhouse effect and lower land albedo.

449   In contrast, geochemical modeling suggests lower global temperatures due to decreased

450 greenhouse gas concentrations when land is positioned in the tropics due to enhanced silicate

451 weathering (Marshall et al. 1988; Worsley and Kidder 1991). While no dynamic carbon cycle

452 was modeled in these experiments, precipitation over the continent in the RECT experiment is

453 extremely low, suggesting that weathering would also be low despite warm tropical continents.

454 Absence of land plants and orography reduce moisture transport over large tropical continents.

455 Precipitation and runoff increases following supercontinental breakup suggest higher weathering

456 rates and a reduction of greenhouse forcing (Donnadieu et al. 2004; 2006). In our experiments,

457 low latitude (≤30°) precipitation rates over land in the MAR simulation are nearly three times

458 higher than in the RECT experiment at 95 and 93% TSI, upholding the conclusion that

20

459   continental fragmentation may be as important as latitudinal position to weathering rates. Apart

460   from affecting precipitation patterns, the absence of land plants in the Neoproterozoic would

461   limit the efficiency of silicate weathering, as root growth, organic acid secretion, and enhanced

462   runoff retention by plants all enhance weathering rates (Berner 1997), though microbial

463   communities on Neoproterozoic continents may have enhanced weathering rates to a lesser

464   extent (Lenton and Watson 2004). Chemical weathering rates may also have been enhanced in

465   fine-grained soils (Keller and Wood 1993) prior to land plant evolution.

466   Rising anthropogenic greenhouse gas emissions highlight the importance of quantifying

467   modern climate sensitivity to changes in radiative forcing. Despite intense study, modern and

468   paleo- climate sensitivities remain difficult to constrain (Roe and Baker 2007; Knutti and Hegerl

469   2008; Rohling et al. 2012). In the absence of long-term observations, paleoclimate archives have

470   been used to estimate climate sensitivity on long time scales in response to changes in

471   greenhouse forcing by comparing changes in proxy CO_2 with proxy temperature (e.g., Royer et

472   al. 2007). A potential problem with this approach is that boundary conditions specific to past

473   time periods may influence climate sensitivity. In fact, our results show the danger of this

474   approach by suggesting geography strongly modulates climate processes and sensitivity. A high

475   degree of land-sea contrast in the tropics increases the importance of direct radiative heating at

476   the expense of greenhouse heating, lowering the climate sensitivity to changes in the water vapor

477   feedback with TSI reductions.

478

479   **5. Conclusions**

480   Our simulations do not support the hypothesis that increased tropical land mass would facilitate

481   initiation of a Snowball Earth event. While raising surface albedo, large tropical landmasses alter

482   the partitioning of energy in the tropics such that global climate is less sensitive to reductions in

483   top of the atmosphere shortwave forcing. The energy budget in AQP has a stronger dependence

484   on greenhouse forcing while the energy budget of MOD-NT, MAR, and RECT show stronger

485   dependence on direct radiative forcing. As greenhouse forcing decreases exponentially with

486   temperature following specific humidity scaling by the Clausius-Clapeyron equation, direct top

487   of the atmosphere shortwave forcing decreases linearly with incremental decreases in TSI. When

488   there is a high degree of land/sea contrast in the deep tropics, an amplified Walker circulation

489   raises tropical temperatures, enhances evaporation over tropical oceans and maintains a stronger

490   greenhouse effect at reduced TSI than when no land is present. Topography also provides a

491   strong control on Snowball Earth initiation. Including topography in a modern continental

492   configuration lowered the TSI threshold for Snowball Earth initiation by up to 2% by altering

493   cloud and snow coverage and the meridional albedo gradient, reducing the equator-to-pole

494   temperature gradient.

495   More generally, this study demonstrates that paleogeography and paleotopography can

496   have a significant impact on climate sensitivity by repartitioning energy in the climate system.

497   This must be considered when using paleoclimate records to estimate climate sensitivity to

498   changing atmospheric CO_2.

499

507

References

509 Abbot, D. S., A. Voigt, and D. Koll, 2011: The Jormungand global climate state and implications
510   for Neoproterozoic glaciations. *J. Geophys. Res*, **116**, doi:10.1029/2011JD015927.

511 Bao, H., I. J. Fairchild, P. M. Wynn, and C. Spötl, 2009: Stretching the envelope of past surface
512   environments: Neoproterozoic glacial lakes from Svalbard. *Science*, **323**, 119–122,
513   doi:10.1371/journal.

514 Bao, H., J. R. Lyons, and C. Zhou, 2008: Triple oxygen isotope evidence for elevated CO_2 levels
515   after a Neoproterozoic glaciation. *Nature*, **453**, 504–506, doi:10.1038/nature06959.

516 Barron, E. J., S. L. Thompson, and W. W. Hay, 1984: Continental distribution as a forcing factor
517   for global-scale temperature. *Nature*, **316**, 574–575.

518 Baum, S., and T. Crowley, 2001: GCM response to Late Precambrian ($\sim$ 590 Ma) ice—covered
519   continents. *Geophys. Res. Lett*, **28**, 583–586.

520 Baum, S., and T. Crowley, 2003: The snow/ice instability as a mechanism for rapid climate
521   change: A Neoproterozoic Snowball Earth model example. *Geophys. Res. Lett*, **30**.

522 Bendtsen, J., 2002: Climate sensitivity to changes in solar insolation in a simple coupled climate
523   model. *Clim Dyn*, **18**, 595–609, doi:10.1007/s00382-001-0198-4.

524 Berner, R. A., 1997: Geochemistry and Geophysics: The Rise of Plants and Their Effect on
525   Weathering and Atmospheric CO2. *Science*, **276**, 544–546,
526   doi:10.1126/science.276.5312.544.

527 Bodiselitsch, B., C. Koeberl, S. Master, and W. Reimold, 2005: Estimating duration and intensity
528   of Neoproterozoic snowball glaciations from Ir anomalies. *Science*, **308**, 239–242.

529 Budyko, M., 1969: The effect of solar radiation variations on the climate of the earth. *Tellus*, **21**,
530   611–619.

531 Chandler, M. A., and L. E. Sohl, 2000: Climate forcings and the initiation of low-latitude ice
532   sheets during the Neoproterozoic Varanger glacial interval. *J. Geophys. Res*, **105**, 20737–
533   20756.

534 Collins, W. D. and Coauthors, 2004: Description of the NCAR community atmosphere model
535   (CAM 3.0). *NCAR Tech. Note NCAR/TN-464+ STR*.

536 Collins, W. D. and Coauthors, 2006: The community climate system model version 3 (CCSM3).

23

537   *Journal of Climate*, **19**, 2122–2143.

538 Crowley, T., and S. Baum, 1993: Effect of decreased solar luminosity on late Precambrian ice
539   extent. *J. Geophys. Res*, **98**, 16723–16732.

540 Dickinson, R. E., A. Henderson-Sellers, and P. J. Kennedy, 1993: Biosphere-atmosphere transfer
541   scheme (BATS) version 1e as coupled to the NCAR community climate model. *NCAR*
542   *Technical Note*, 1–80.

543 Donnadieu, Y., Y. Goddéris, G. Ramstein, A. Nedelec, and J. Meert, 2004: A "snowball Earth"
544   climate triggered by continental break-up through changes in runoff. *Nature*, **428**, 303–306.

545 Donnadieu, Y., Y. Goddéris, R. Pierrehumbert, G. Dromart, F. Fluteau, and R. Jacob, 2006: A
546   GEOCLIM simulation of climatic and biogeochemical consequences of Pangea breakup.
547   *Geochem. Geophys. Geosyst*, **7**, Q11019, doi:10.1029/2006GC001278.

548 Gough, D., 1981: Solar interior structure and luminosity variations. *Sol Phys*, **74**, 21–34.

549 Hansen, J., G. Russell, D. Rind, P. Stone, A. Lacis, S. Lebedeff, R. Ruedy, and L. Travis, 1983:
550   Efficient three-dimensional global models for climate studies: Models I and II. *Monthly*
551   *Weather Review*, **111**, 609–662.

552 Hartmann, D., 1994: *Global Physical Climatology*. Academic Press, 1 pp.

553 Held, I., and B. Soden, 2000: Water Vapor Feedback and Global Warming. *Annual Review of*
554   *Energy and the Environment*, **25**, 441–475.

555 Hoffman, P., and D. Schrag, 2002: The snowball Earth hypothesis: testing the limits of global
556   change. *Terra Nova*, **14**, 129–155.

557 Hoffman, P., and Z. Li, 2009: A palaeogeographic context for Neoproterozoic glaciation.
558   *Palaeogeography, Palaeoclimatology, Palaeoecology*, **277**, 158–172.

559 Hyde, W., T. Crowley, S. Baum, and W. Peltier, 2000: Neoproterozoic "Snowball Earth"
560   simulations with a coupled climate/ice-sheet model. *Nature*, **405**, 425–429.

561 Keller, C. K., and B. D. Wood, 1993: Possibility of chemical weathering before the advent of
562   vascular land plants.

563 Kirschvink, J. L., 1992: Late Proterozoic low-latitude global glaciation: the snowball Earth. *The*
564   *Proterozoic Biosphere*, **52**.

565 Knauth, L. P., and M. J. Kennedy, 2009: The late Precambrian greening of the Earth. *Nature*,
566   **460**, 728–732, doi:10.1038/nature08213.

567 Knutti, R., and G. C. Hegerl, 2008: The equilibrium sensitivity of the Earth's temperature to
568   radiation changes. *Nature Publishing Group*, **1**, 735–743.

569 Lenton, T. M., and A. J. Watson, 2004: Biotic enhancement of weathering, atmospheric oxygen

570   and carbon dioxide in the Neoproterozoic. *Geophys Res Lett*, **31**, L05202,
571   doi:10.1029/2003GL018802.

572   Li, Z. and Coauthors, 2008: Assembly, configuration, and break-up history of Rodinia: A
573   synthesis. *Precambrian Research*, **160**, 179–210.

574   Love, G. D. and Coauthors, 2008: Fossil steroids record the appearance of Demospongiae during
575   the Cryogenian period. *Nature*, **457**, 718–721, doi:10.1038/nature07673.

576   Macdonald, F. A. and Coauthors, 2010: Calibrating the Cryogenian. *Science*, **327**, 1241–1243,
577   doi:10.1126/science.1183325.

578   Marshall, H., J. Walker, and W. Kuhn, 1988: Long-Term Climate Change and the Geochemical
579   Cycle of Carbon. *J Geophys Res-Atmos*, **93**, 791–801.

580   Micheels, A., and M. Montenari, 2008: A snowball Earth versus a slushball Earth: Results from
581   Neoproterozoic climate modeling sensitivity experiments. *Geosphere*, **4**, 401,
582   doi:10.1130/GES00098.1.

583   Myhre, G., E. J. Highwood, K. P. Shine, and F. Stordal, 1998: New estimates of radiative forcing
584   due to well mixed greenhouse gases. *Geophys. Res. Lett*, **25**, 2715–2718.

585   North, G. R., 1975a: Analytical solution to a simple climate model with diffusive heat transport.
586   *Journal of the Atmospheric Sciences*, **32**, 1301–1307.

587   North, G. R., 1975b: Theory of energy-balance climate models. *J. Atmos. Sci*, **32**, 2033–2043.

588   Oleson, K. and Coauthors, 2004: Technical description of the Community Land Model (CLM).
589   186.

590   Pierrehumbert, R. T., D. Abbot, A. Voigt, and D. Koll, 2011: Climate of the Neoproterozoic.
591   *Annual Reviews of Earth and Planetary Sciences*, **39**, 417–460, doi:10.1146/annurev-earth-
592   040809-152447.

593   Poulsen, C. J., 2003: Absence of a runaway ice-albedo feedback in the Neoproterozoic. *Geol*, **31**,
594   473–476.

595   Poulsen, C. J., and R. Jacob, 2004: Factors that inhibit snowball Earth simulation.
596   *Paleoceanography*, **19**.

597   Poulsen, C. J., R. Jacob, R. Pierrehumbert, and T. Huynh, 2002: Testing paleogeographic
598   controls on a Neoproterozoic snowball Earth. *Geophys. Res. Lett*, **29**, 1515–1518.

599   Poulsen, C. J., R. Pierrehumbert, and R. Jacob, 2001: Impact of ocean dynamics on the
600   simulation of the Neoproterozoic "snowball Earth." *Geophys. Res. Lett*, **28**, 1575–1578.

601   Ridgwell, A. J., M. J. Kennedy, and K. Caldeira, 2003: Carbonate deposition, climate stability,
602   and Neoproterozoic ice ages. *Science*, **302**, 859–862, doi:10.1126/science.1088342.

603   Roe, G., and M. Baker, 2007: Why is climate sensitivity so unpredictable? *Science*, **318**, 629–
604   632.

605   Roeckner, E. and Coauthors, 2003: The atmospheric general circulation model ECHAM5: Part 1:
606   Model description.

607   Rohling, E. J. and Coauthors, 2012: Making sense of palaeoclimate sensitivity. *Nature*, **491**,
608   683–691, doi:10.1038/nature11574.

609   Rose, B. E. J., and J. Marshall, 2009: Ocean Heat Transport, Sea Ice, and Multiple Climate
610   States: Insights from Energy Balance Models. *Journal of the Atmospheric Sciences*, **66**,
611   2828–2843, doi:10.1175/2009JAS3039.1.

612   Royer, D. L., R. A. Berner, and J. Park, 2007: Climate sensitivity constrained by CO2
613   concentrations over the past 420 million years. *Nature*, **446**, 530–532,
614   doi:10.1038/nature05699.

615   Sellers, W. D., 1969: A global climatic model based on the energy balance of the earth-
616   atmosphere system. *Journal of Applied Meteorology*, **8**, 392–400.

617   Shields, G. A., 2005: Neoproterozoic cap carbonates: a critical appraisal of existing models and
618   the plumeworld hypothesis. *Terra Nova*, **17**, 299–310, doi:10.1111/j.1365-
619   3121.2005.00638.x.

620   Voigt, A., and J. Marotzke, 2009: The transition from the present-day climate to a modern
621   Snowball Earth. *Clim Dyn*, **35**, 887–905, doi:10.1007/s00382-009-0633-5.

622   Voigt, A., D. S. Abbot, R. T. Pierrehumbert, and J. Marotzke, 2011: Initiation of a Marinoan
623   Snowball Earth in a state-of-the-art atmosphere-ocean general circulation model. *Climate of*
624   *the Past*, **7**, 249–263, doi:10.5194/cp-7-249-2011.
625   http://pubman.mpdl.mpg.de/pubman/item/escidoc:993585:2/component/escidoc:993584/cp-
626   7-249-2011.pdf.

627   Waldbauer, J. R., L. S. Sherman, D. Y. Sumner, and R. E. Summons, 2009: Late Archean
628   molecular fossils from the Transvaal Supergroup record the antiquity of microbial diversity
629   and aerobiosis. *Precambrian Research*, 1–20, doi:10.1016/j.precamres.2008.10.011.

630   Worsley, T. R., and D. L. Kidder, 1991: First-order coupling of paleogeography and CO2, with
631   global surface temperature and its latitudinal contrast. *Geol*, **19**, 1161–1164.

632   Yang, J., W. R. Peltier, and Y. Hu, 2012a: The Initiation of Modern "Soft Snowball" and 'Hard
633   Snowball' Climates in CCSM3. Part I: The Influences of Solar Luminosity, CO
634   2Concentration, and the Sea Ice/Snow Albedo Parameterization. *Journal of Climate*, **25**,
635   2711–2736, doi:10.1175/JCLI-D-11-00189.1.

636   Yang, J., W. R. Peltier, and Y. Hu, 2012b: The Initiation of Modern "Soft Snowball" and 'Hard
637   Snowball' Climates in CCSM3. Part II: Climate Dynamic Feedbacks. *Journal of Climate*, **25**,
638   2737–2754, doi:10.1175/JCLI-D-11-00190.1.

639

Tables

Configuration	TSI (% of modern)	Years Run	Result
Aquaplanet (AQP)	100	400-530	Ice latitude of 39.1°S, 39.5°N
	99	400-500	Ice latitude of 35.2°S, 35.7°N
	97	400-651	Ice latitude of 20.4°S, 22.7°N
	95	400-567	Ice latitude of 15.0°S, 16.0°N
	93	400-553	Ice latitude of 12.2°S, 13.0°N
	92	400-595	Ice latitude of 9.4°S, 10.6°N
	91	400-525	Snowball by year 485
	90	400-511	Snowball by year 431
	88	400-575	Snowball by year 420
	85	400-511	Snowball by year 414
	80	400-539	Snowball by year 410
Modern – no topography (MOD-NT)	100	400-507	Ice latitude of 41.1°S, 42.1°N
	97	500-569	Ice latitude of 33.0°S, 36.0°N
	95	500-653	Ice latitude of 26.5°S, 30.0°N
	93	500-620	Ice latitude of 20.1°S, 23.7°N
	90	500-625	Ice latitude of 14.5°S, 17.4°N
	89	500-611	Ice latitude of 12.5°S, 15.5°N
	88	500-697	Ice latitude of 10.0°S, 11.8°N
	87	500-647	Snowball by year 534
	85	500-611	Snowball by year 511
	80	500-611	Snowball by year 505
Marinoan (MAR)	100	400-539	Ice latitude of 40.6°S, 39.3°N
	97	499-602	Ice latitude of 34.6°S, 32.2°N
	95	499-655	Ice latitude of 30.4°S, 27.4°N
	93	499-610	Ice latitude of 26.9°S, 23.2°N
	90	499-617	Ice latitude of 21.5°S, 18.1°N
	88	499-681	Ice latitude of 18.1°S, 14.4°N
	87	499-723	Ice latitude of 15.8°S, 12.9°N
	86	499-674	Ice latitude of 13.6°S, 10.5°N
	85	499-652	Snowball by year 572
	80	499-638	Snowball by year 504
Rectangle (RECT)	100	400-537	Ice latitude of 38.8°S, 39.1°N
	97	510-565	Ice latitude of 33.3°S, 33.7°N
	95	510-635	Ice latitude of 29.8°S, 29.9°N
	93	510-579	Ice latitude of 26.0°S, 26.4°N
	90	510-635	Ice latitude of 20.6°S, 21.4°N
	88	510-635	Ice latitude of 17.3°S, 18.0°N
	85	510-663	Ice latitude of 10.2°S, 12.4°N
	84	510-772	Snowball by year 533

	83	510-642	Snowball by year 519
	80	510-621	Snowball by year 515
Modern – modern topography (MOD-WT)	100	1-142	Ice latitude of 41.4°S, 38.6°N
	97	101-209	Ice latitude of 28.1°S, 30.8°N
	95	101-222	Ice latitude of 22.2°S, 25.2°N
	93	101-219	Ice latitude of 18.4°S, 20.7°N
	90	101-250	Ice latitude of 11.4°S, 15.0°N
	89	101-422	Snowball by year 198
	88	101-310	Snowball by year 124
	85	101-229	Snowball by year 110
	80	101-242	Snowball by year 107

641 **Table 1.** Summary of model experiments performed and result of run when terminated after

642 years indicated. TSI is listed as a percentage of the modern value.

	Continental Arrangement			
Variable	**AQP**	**MOD-NT**	**MAR**	**RECT**
Land Fraction, global	0	0.323	0.278	0.270
Land Fraction, 30°N/S	0	0.288	0.481	0.385
Surface Albedo	0.310	0.326	0.356	0.353
Planetary Albedo	0.406	0.397	0.403	0.402
Mean Surface Temperature (K)	273.4	274.0	272.6	272.4
Mean Annual Ice Latitude	39.5°N, 39.1°S	42.1°N, 41.1°S	39.3°N, 40.6°S	39.1°N, 38.8°S

643 **Table 2.** Results for AQP, MOD-NT, MAR, and RECT configurations at 100% TSI.

644

645 **Figure Captions**

646

647 **Figure 1.** Surface temperature contour plots at 100% (left column) and 95% TSI (right column)

648 for the AQP (top), MOD-NT, MAR, and RECT (bottom) experiments. Temperature structures

649 are highly zonal, with some asymmetries near land-ocean transitions. At 100% TSI, the four

650 geographies have a highly similar temperature structure with mean annual tropical and polar

651 temperatures around 295K and 225K respectively. At 95% TSI, the temperature structures of the

652 four geographies diverge – AQP averages at least 15K colder than the MOD-NT, MAR, and

653 RECT geographies at all latitudes.

654

655   **Figure 2.** Mean annual surface temperature (a), mean annual ice margin (b), and surface (c) and

656   planetary (d) albedos as a function of TSI. A strong bifurcation notes the transition to a snowball

657   state for each configuration as TSI is decreased. AQP enters the snowball state most readily (TSI

658   < 92%), followed by MOD-NT, MAR, and RECT when TSI is reduced below 88%, 86%, and

659   85% respectively.

660

661   **Figure 3.** Components of surface energy balance at 100% TSI for all four geographies. (a) Net

662   surface shortwave radiation absorbed, (b) net surface longwave radiation emitted, (c) total cloud

663   forcing, (d) total greenhouse forcing (difference in upwelling clearsky longwave radiation at the

664   top of the atmosphere and the surface), and (e) cloud forcing over the ocean. All plots are in W

665   m^{-2}. Geographies with large amounts of tropical land area (i.e., MAR and RECT) have higher net

666   shortwave in the deep tropics than geographies with little or no tropical land area (i.e., AQP)

667   primarily due to a lower cloud fraction. This energy disparity is ameliorated by increased

668   longwave emission and a smaller greenhouse forcing for the high land configurations, leading to

669   similar tropical temperatures across all four geographies.

670

671   **Figure 4.** Total annual average cloud fraction for all four geographies at 100% TSI. Cloud

672   fractions are highest over regions of vigorous convection over the ocean and lower in the

673   subtropics and particularly over land. Cloud fractions are notably low over MAR and RECT

674   geographies due to the presence of large continents in the subtropics, though cloud fractions are

675   low over the entirety of the RECT continent, while cloud fractions remain higher in the deep

676   tropics over the smaller continents of the MAR geography.

677

678   **Figure 5.** Weighted area average (from 30°N/S) components of the surface energy balance as a

679   function of TSI for all four geographies. (a) Net surface shortwave radiation absorbed, (b) net

680   surface longwave radiation emitted, (c) total cloud forcing, and (d) total greenhouse forcing

681   (difference in upwelling clearsky longwave radiation at the top of the atmosphere and the

682   surface). All plots are in W m^{-2}. At 100% TSI, the AQP and MOD-NT configurations are more

683   reliant on greenhouse forcing to maintain tropical temperatures, and are most sensitive to

684   decreases in TSI as the amount of atmospheric water vapor decreases with TSI. Cloud forcing in

685   the MAR and RECT configurations are more positive by ~10 W m^{-2} prior to Snowball initiation,

686   and higher absorbed shortwave fluxes that decrease less rapidly than greenhouse forcing.

687

688   **Figure 6.** Vertically integrated water vapor as a function of (a) average global surface

689   temperature (K) and (b) TSI from 30°N/S for all four geographies. At 100% TSI, vertically

690   integrated water vapor is notably lower for high tropical land configurations MAR and RECT,

691   with the RECT geography having 35% less tropical atmospheric water vapor than the AQP

692   geography. Temperature and specific humidity are tightly coupled (a), as vertically integrated

693   water vapor flows average global surface temperature as suggested by the Clausius-Clapeyron

694   equation. As TSI is reduced however, the rate of decrease of vertically integrated water vapor (b)

695   is higher for AQP than the other configurations with land since the energy budget has a larger

696   greenhouse forcing term.

697

698   **Figure 7.** Annually and meridionally (5°N/S) averaged longitudinal/height cross-sections of

699   vertical pressure velocities (mb day^{-1}) and relative humidity (%) for the AQP (a,c) and RECT

700   (b,d) geographies at 95% TSI. Black contour lines in b and d indicate specific humidity in 1 g kg$^-$

701   ^{1} intervals. Vertical pressure velocities in the AQP configuration are ubiquitously negative in the

702   troposphere, suggesting vigorous upward motion at all longitudes in the annual average. In

703   contrast, the RECT configuration shows strong upward motion over the oceans, but strong

704   subsidence in the free troposphere limiting weaker upward motion to the boundary layer over the

705   continent. Likewise, the troposphere is near saturation at the surface and near the tropopause in

706   the AQP experiment at all longitudes while the troposphere is near saturation in the boundary

707   layer and tropopause over the ocean, but is markedly drier over the continent, particularly over

708   the continent's western half. Over the ocean, near surface specific humidity is nearly three times

709   higher in the RECT experiment than in the AQP experiment. Additionally, higher specific

710   humidity in the middle-troposphere of the RECT experiment results in greenhouse forcing less

711   sensitive to TSI than in the AQP case.

712

713   **Figure 8.** (a) Total surface water flux (Pg s^{-1}) and (b) surface water flux normalized by ocean

714   fraction (Pg s^{-1} ocean fraction^{-1}) from 30°N/S for all four geographies as a function of TSI. At

715   100% TSI, surface water flux is highest for the AQP configuration but falls most rapidly with

716   TSI. Surface water flux normalized by ocean fraction shows evaporation in tropical oceans is

717   more efficient for the MAR and RECT configurations than for the AQP configurations.

718

719   **Figure 9.** Difference between RECT and AQP vertical cloud fractions at 95% TSI. Both zonally

720   averaged differences (a) and longitudinal differences in the deep tropics (b, 10°N/S) are shown.

721   Contour interval is 0.05 and negative values are shaded. The Walker circulation simulated

722   decreases the amount of low- and midlevel clouds and increases the amount of high-level clouds,

723   increasing the shortwave cloud forcing in the tropics by 20-40 W m^{-2} while only decreasing the

724   longwave cloud forcing by 10-15 W m^{-2}.

725

726   **Figure 10.** (a) Mean annual surface temperature (K) and (b) ice margin latitude for the MOD-

727   WT and MOD-NT experiments as a function of TSI. Albedos are tightly coupled to temperature

728   and are not shown. Adding topography to the MOD-NT continental configuration raises the

729   snowball bifurcation point from 88% to 90% modern TSI, though above the bifurcation points,

730   little difference exists between global surface temperature and ice margin latitude.

731

732   **Figure 11**. Contour difference plots between MOD-WT and MOD-NT for (a) surface

733   temperature (K), (b) planetary albedo, (c) cloud fraction, and (d) snow depth (meters liquid water

734   equivalent) at 90% TSI. Adding topography reduces the equator-to-pole temperature gradient (a)

735   by raising subtropical albedo and lowering midlatitude albedo (b), particularly in the Northern

736   Hemisphere where the majority of modern land is located. Albedo changes are driven by changes

737   in cloud cover and snow depth (c and d).
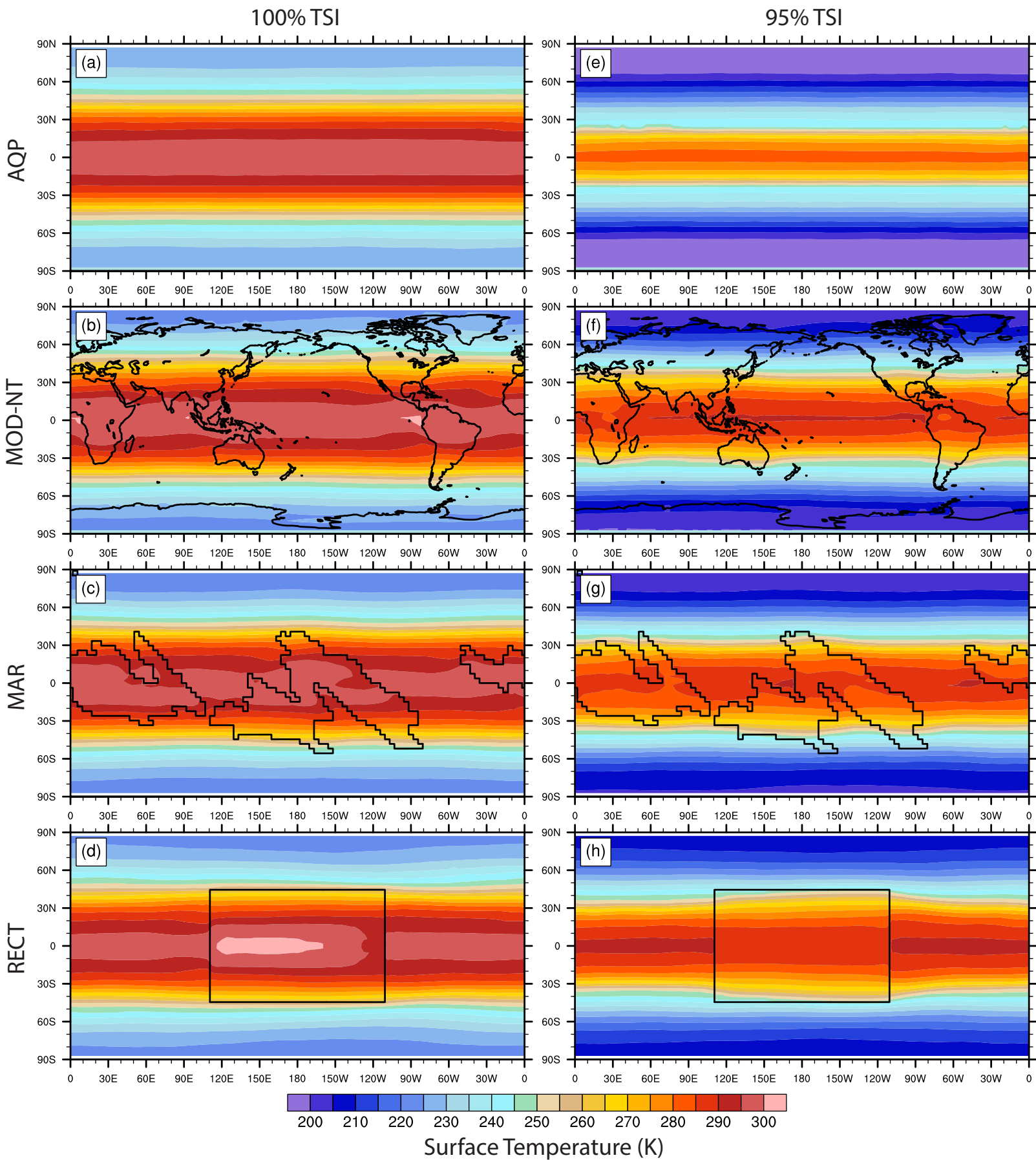
Figure 1. Surface temperature contour plots at 100% (left column) and 95% TSI (right column) for the AQP (top), MOD-NT, MAR, and RECT (bottom) experiments. Temperature structures are highly zonal, with some asymmetries near land-ocean transitions. At 100% TSI, the four geographies have a highly similar temperature structure with mean annual tropical and polar temperatures around 295K and 225K respectively. At 95% TSI, the temperature structures of the four geographies diverge – AQP averages at least 15K colder than the MOD-NT, MAR, and RECT geographies at all latitudes.
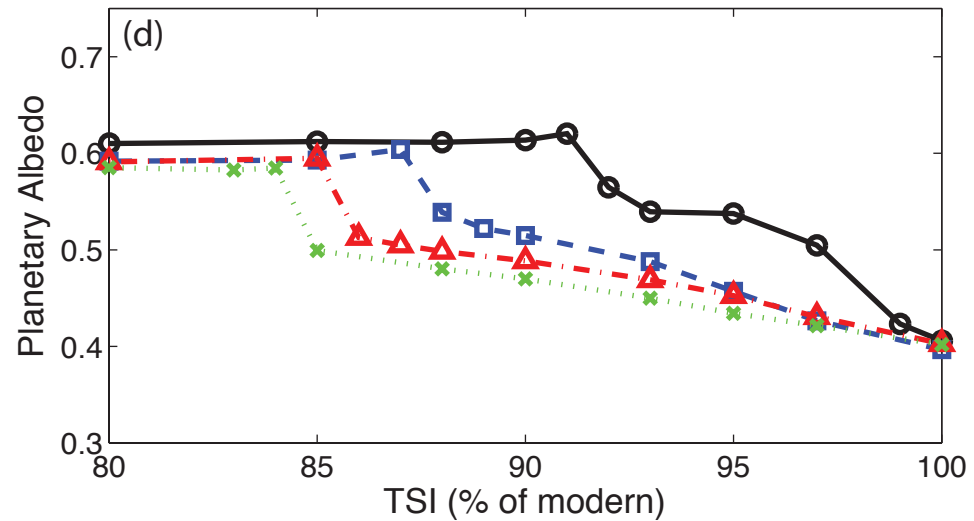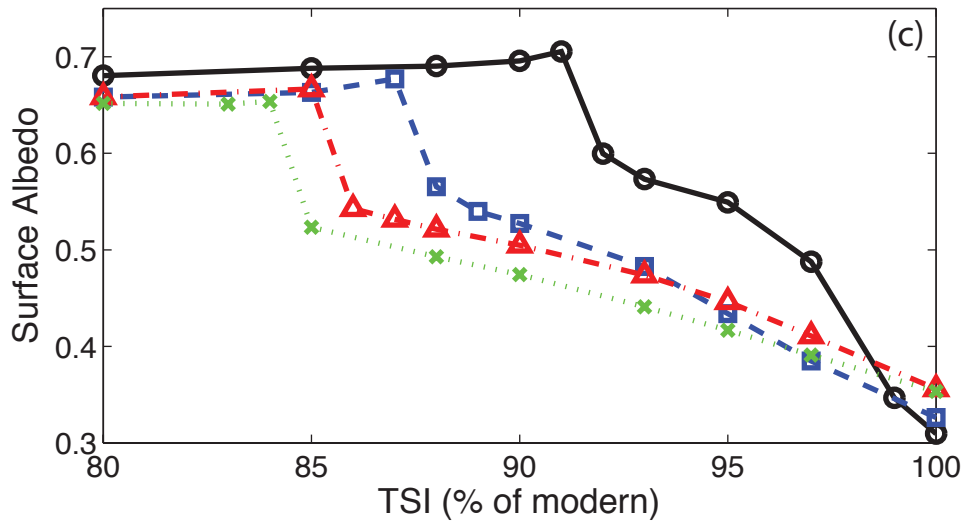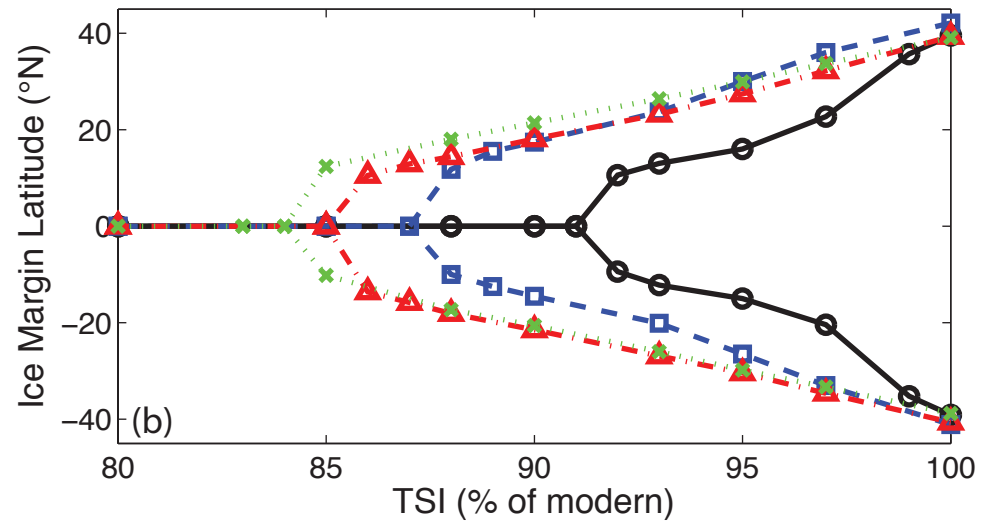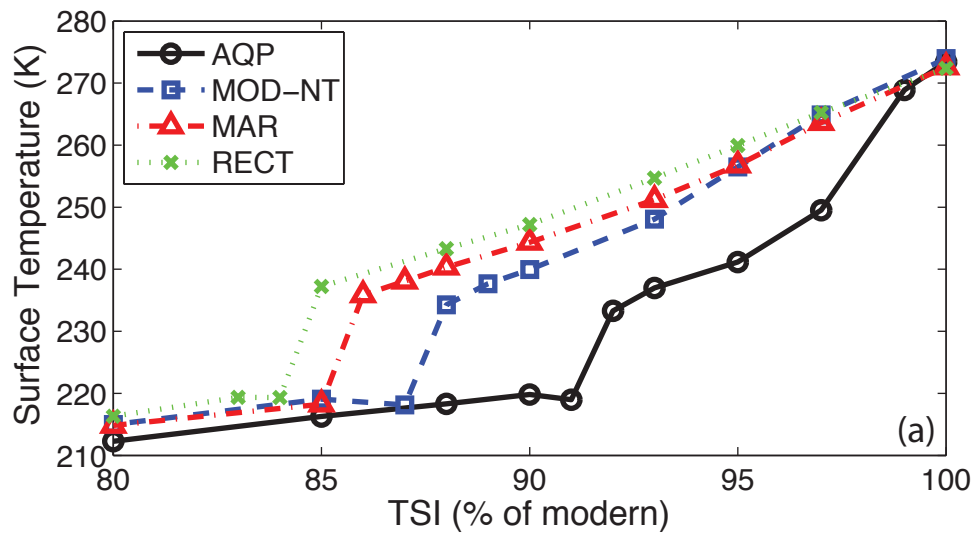
Figure 2. Mean annual surface temperature (a), mean annual ice margin (b), and surface (c) and planetary (d) albedos as a function of TSI. A strong bifurcation notes the transition to a snowball state for each configuration as TSI is decreased. AQP enters the snowball state most readily (TSI < 92%), followed by MOD-NT, MAR, and RECT when TSI is reduced below 88%, 86%, and 85% respectively.
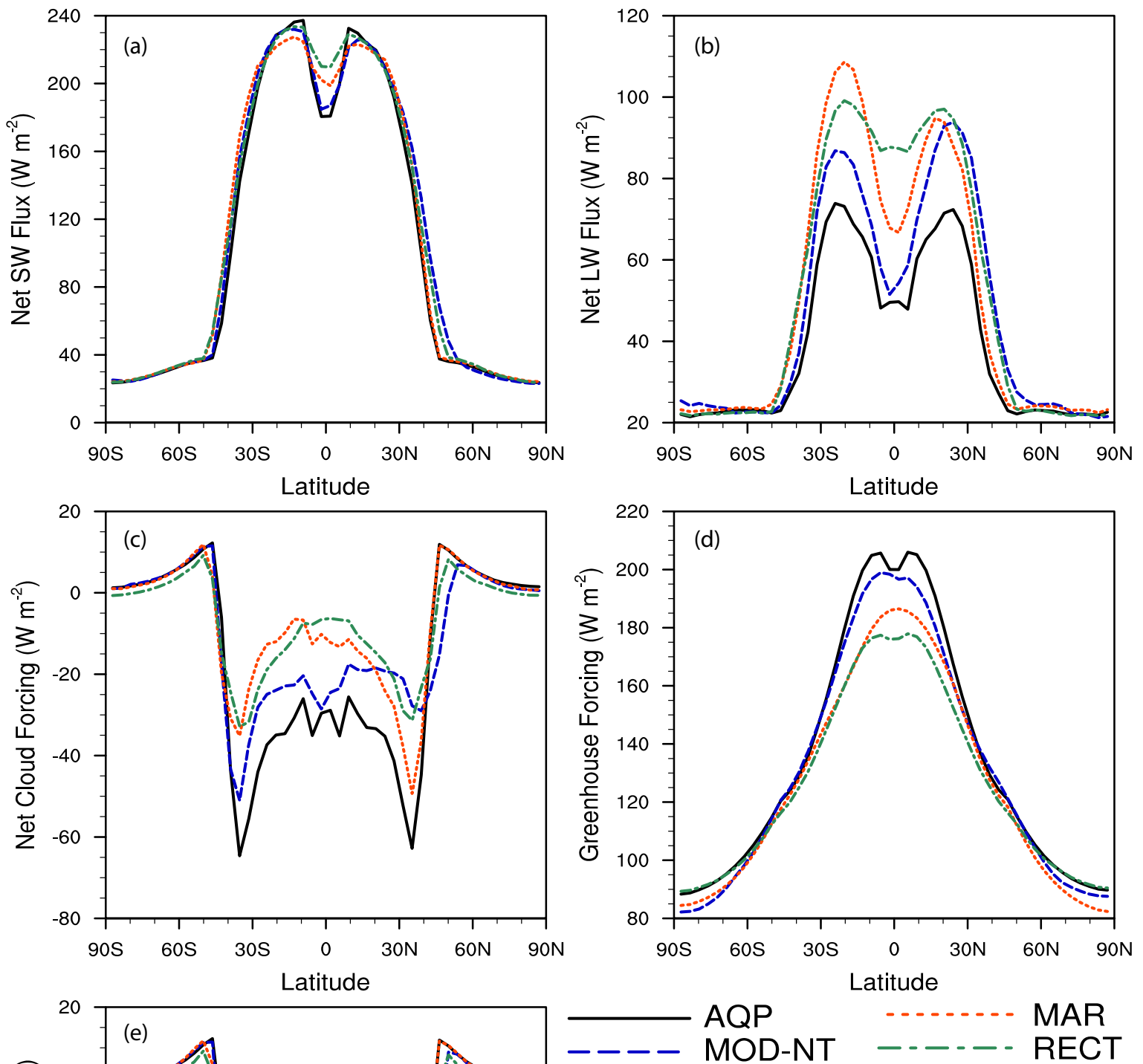
Figure 3. Components of surface energy balance at 100% TSI for all four geographies. (a) Net surface shortwave radiation absorbed, (b) net surface longwave radiation emitted, (c) total cloud forcing, (d) total greenhouse forcing (difference in upwelling clearsky longwave radiation at the top of the atmosphere and the surface), and (e) cloud forcing over the ocean. All plots are in W m⁻². Geographies with large amounts of tropical land area (i.e., MAR and RECT) have higher net shortwave in the deep tropics than geographies with little or no tropical land area (i.e., AQP) primarily due to a lower cloud fraction. This energy disparity is ameliorated by increased longwave emission and a smaller greenhouse forcing for the high land configurations, leading to similar tropical temperatures across all four geographies.
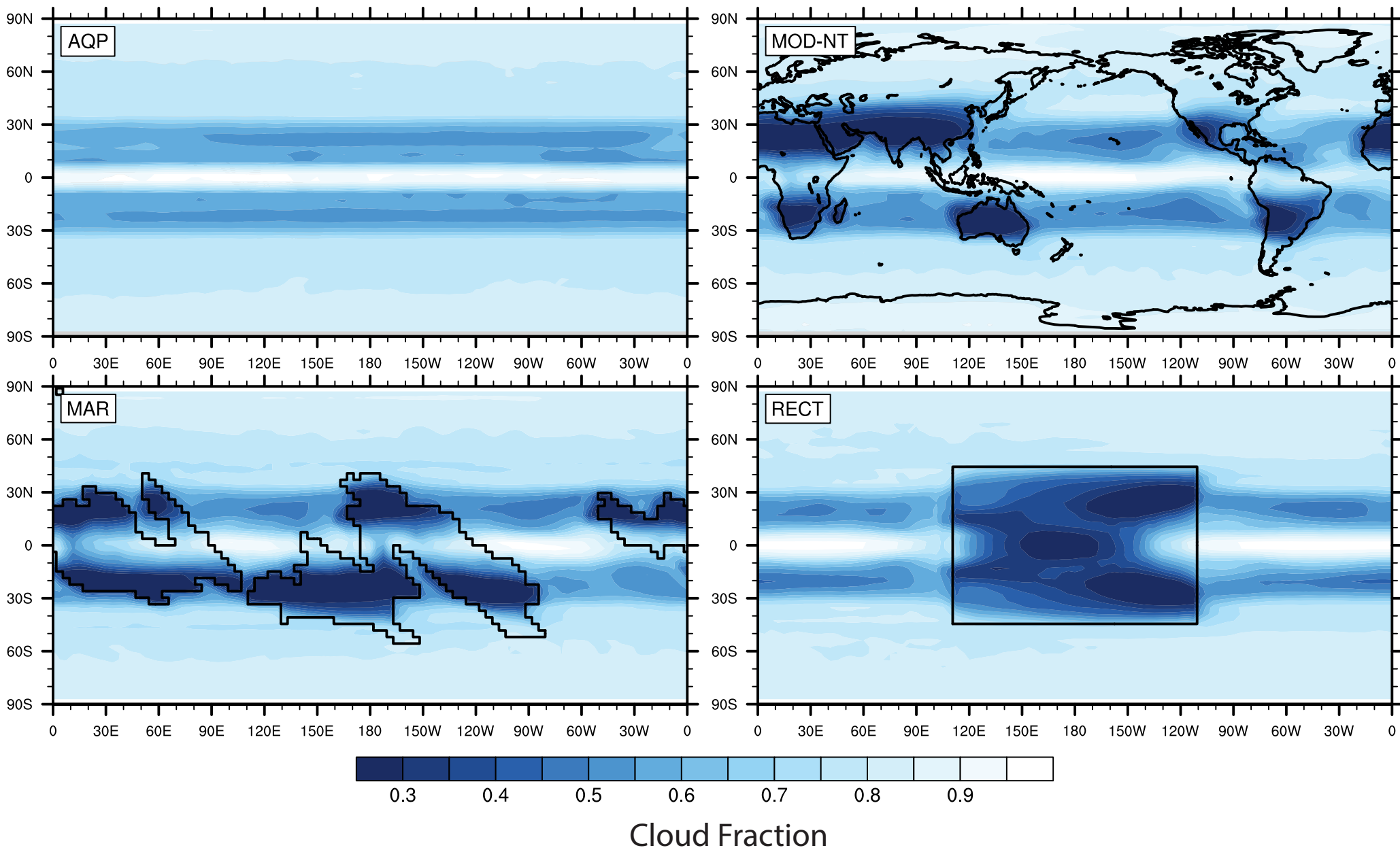
Figure 4. Total annual average cloud fraction for all four geographies at 100% TSI. Cloud fractions are highest over regions of vigorous convection over the ocean and lower in the subtropics and particularly over land. Cloud fractions are notably low over MAR and RECT geographies due to the presence of large continents in the subtropics, though cloud fractions are low over the entirety of the RECT continent, while cloud fractions remain higher in the deep tropics over the smaller continents of the MAR geography.
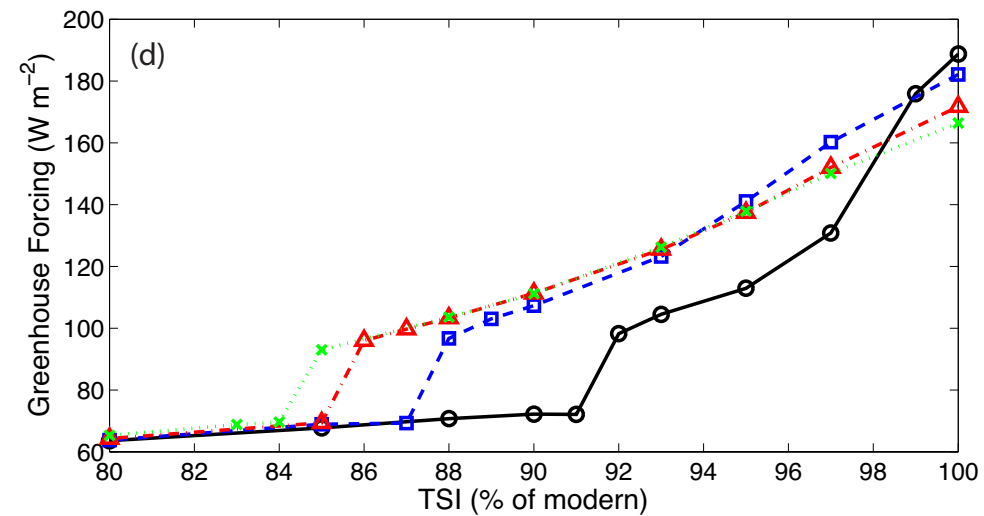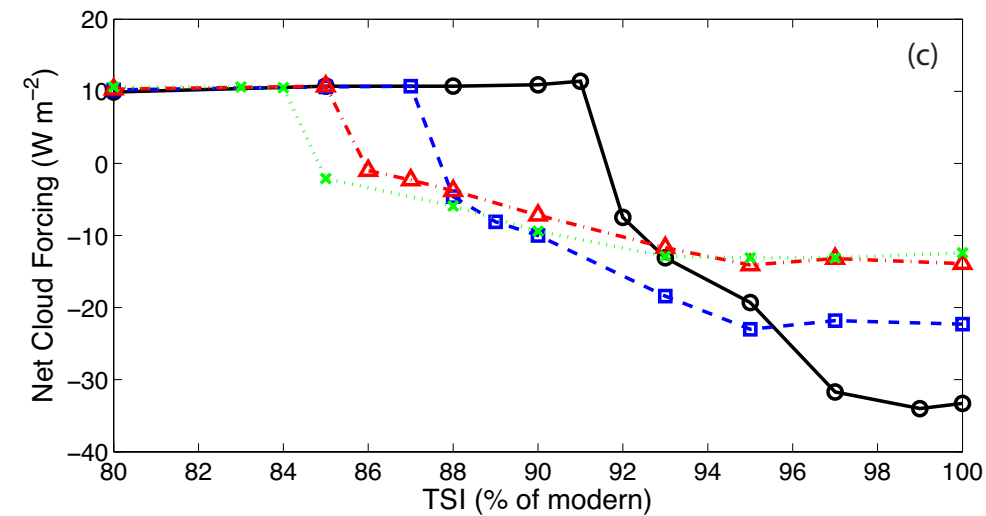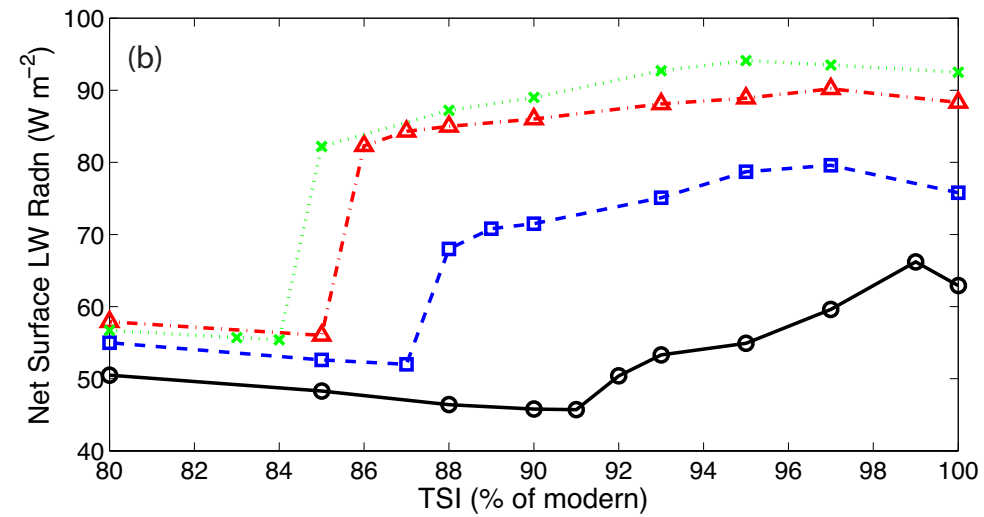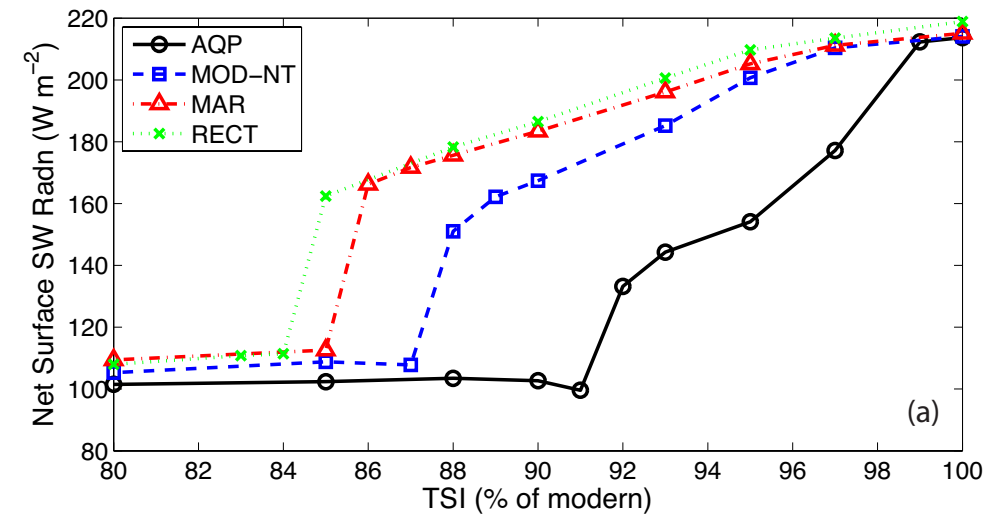
Figure 5. Weighted area average (from 30°N/S) components of the surface energy balance as a function of TSI for all four geographies. (a) Net surface shortwave radiation absorbed, (b) net surface longwave radiation emitted, (c) total cloud forcing, and (d) total greenhouse forcing (difference in upwelling clearsky longwave radiation at the top of the atmosphere and the surface). All plots are in W m⁻². At 100% TSI, the AQP and MOD-NT configurations are more reliant on greenhouse forcing to maintain tropical temperatures, and are most sensitive to decreases in TSI as the amount of atmospheric water vapor decreases with TSI. Before snowball initiation, cloud forcing increases modestly for the AQP and MOD-NT configurations as TSI is reduced, but not enough to overcome the rapid decrease in greenhouse forcing. In contrast, the MAR and RECT configurations show cloud forcings that are more positive by ~10 W m⁻² prior to snowball initiation, and higher absorbed shortwave fluxes that decrease less rapidly than greenhouse forcing.
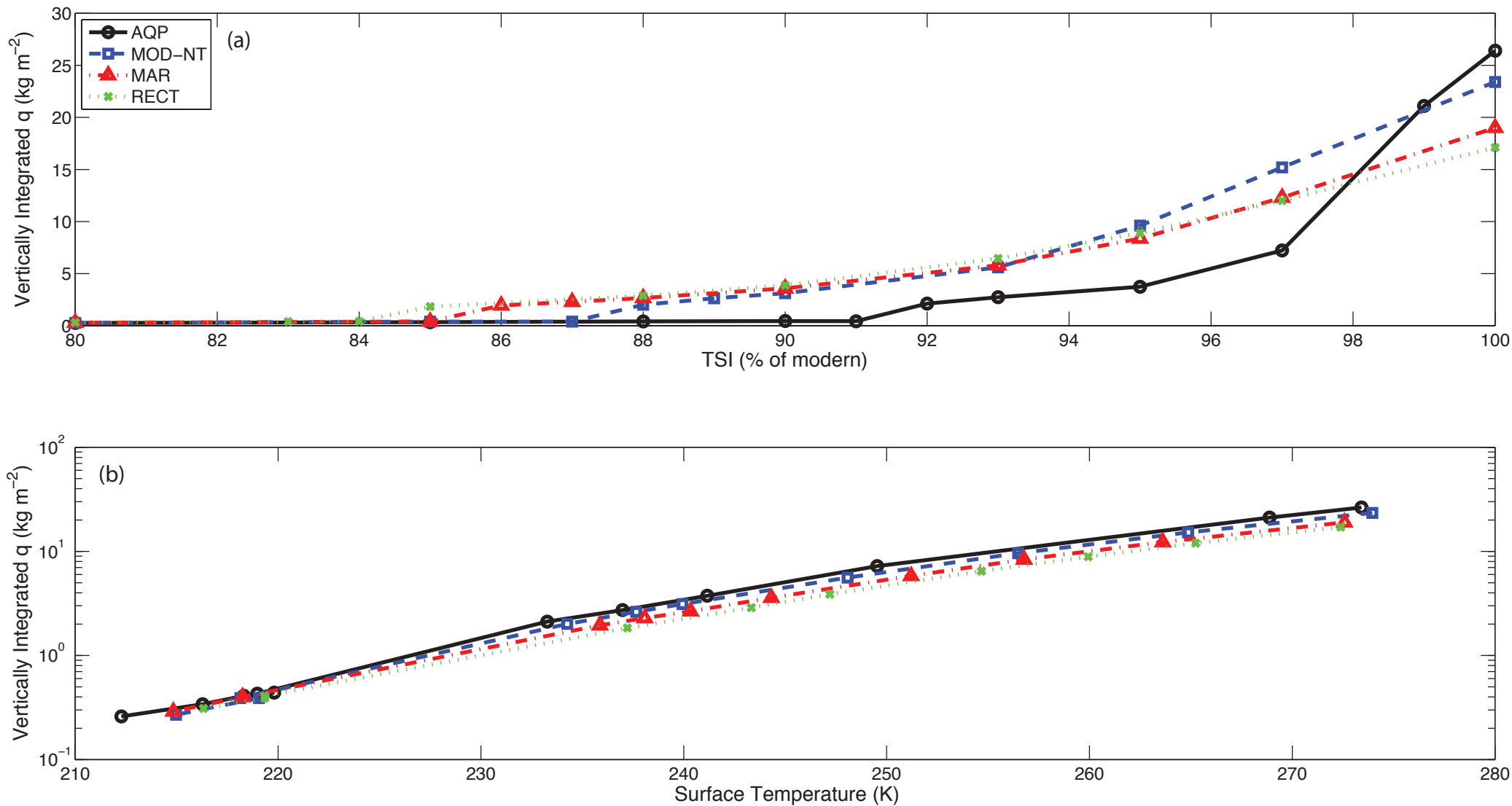
Figure 6. Vertically integrated water vapor as a function of (a) average global surface temperature (K) and (b) TSI from 30°N/S for all four geographies. At 100% TSI, vertically integrated water vapor is notably lower for high tropical land configurations MAR and RECT, with the RECT geography having 35% less tropical atmospheric water vapor than the AQP geography. Temperature and specific humidity are tightly coupled (a), as vertically integrated water vapor follows average global surface temperature as suggested by the Clausius-Clapeyron equation. As TSI is reduced however, the rate of decrease of vertically integrated water vapor (b) is higher for AQP than the other configurations with land since the energy budget has a larger greenhouse forcing term.
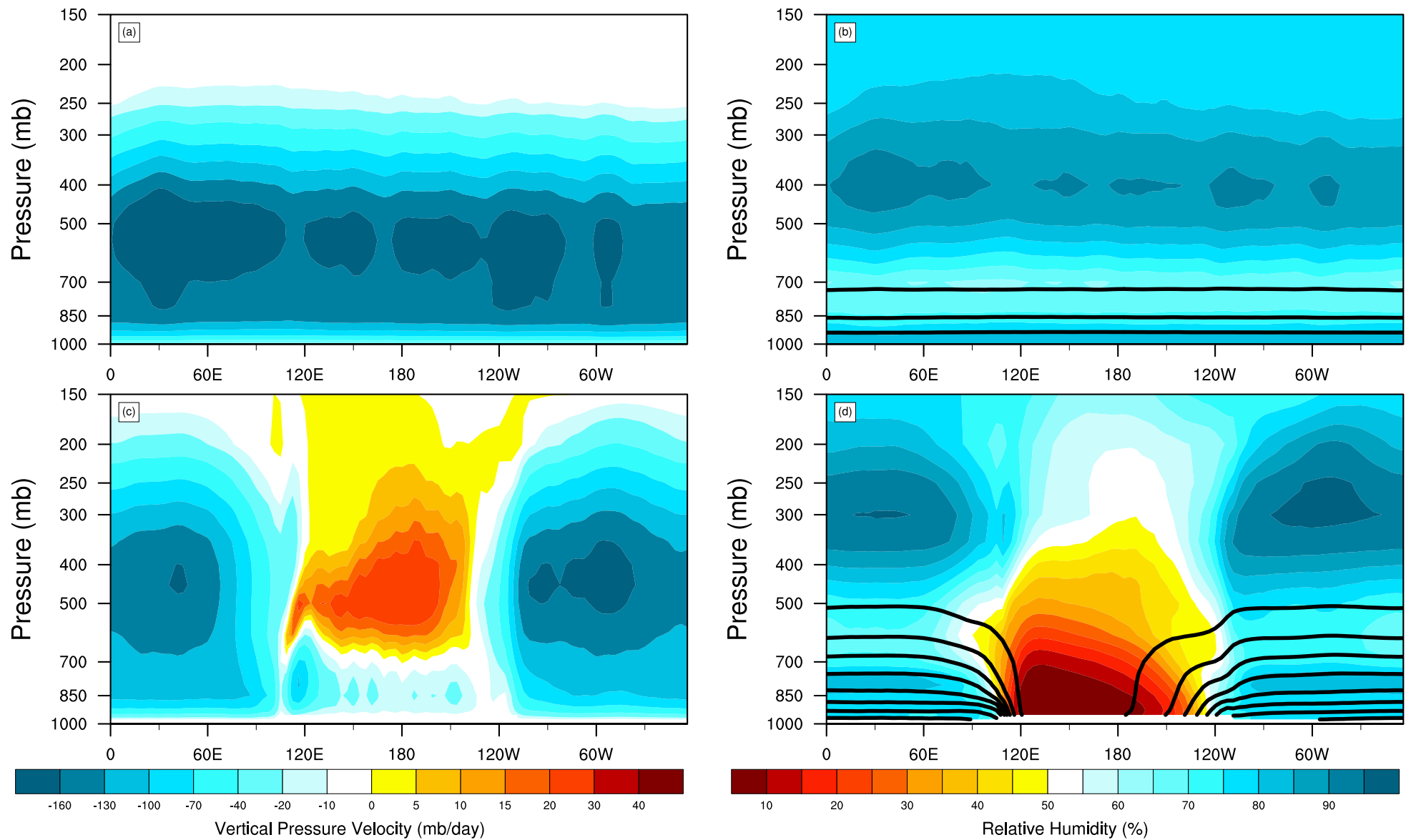
Figure 7. Annually and meridionally (5°N/S) averaged longitudinal/height cross-sections of vertical pressure velocities (mb/day) and relative humidity (%) for the AQP (a,c) and RECT (b,d) geographies at 95% TSI. Black contour lines in b and d indicate specific humidity in 1 g/kg intervals. Vertical pressure velocities in the AQP configuration are ubiquitously negative in the troposphere, suggesting vigorous upward motion at all longitudes in the annual average. In contrast, the RECT configuration shows strong upward motion over the oceans, but strong subsidence in the free troposphere limiting weaker upward motion to the boundary layer over the continent. Likewise, the troposphere is near saturation at the surface and near the tropopause in the AQP experiment at all longitudes while the troposphere is near saturation in the boundary layer and tropopause over the ocean, but is markedly drier over the continent, particularly over the continent's western half. Over the ocean, near surface specific humidity is nearly three times higher in the RECT experiment than in the AQP experiment. Additionally, higher specific humidity in the mid-troposphere of the RECT experiment results in greenhouse forcing less sensitive to TSI than in the AQP case.
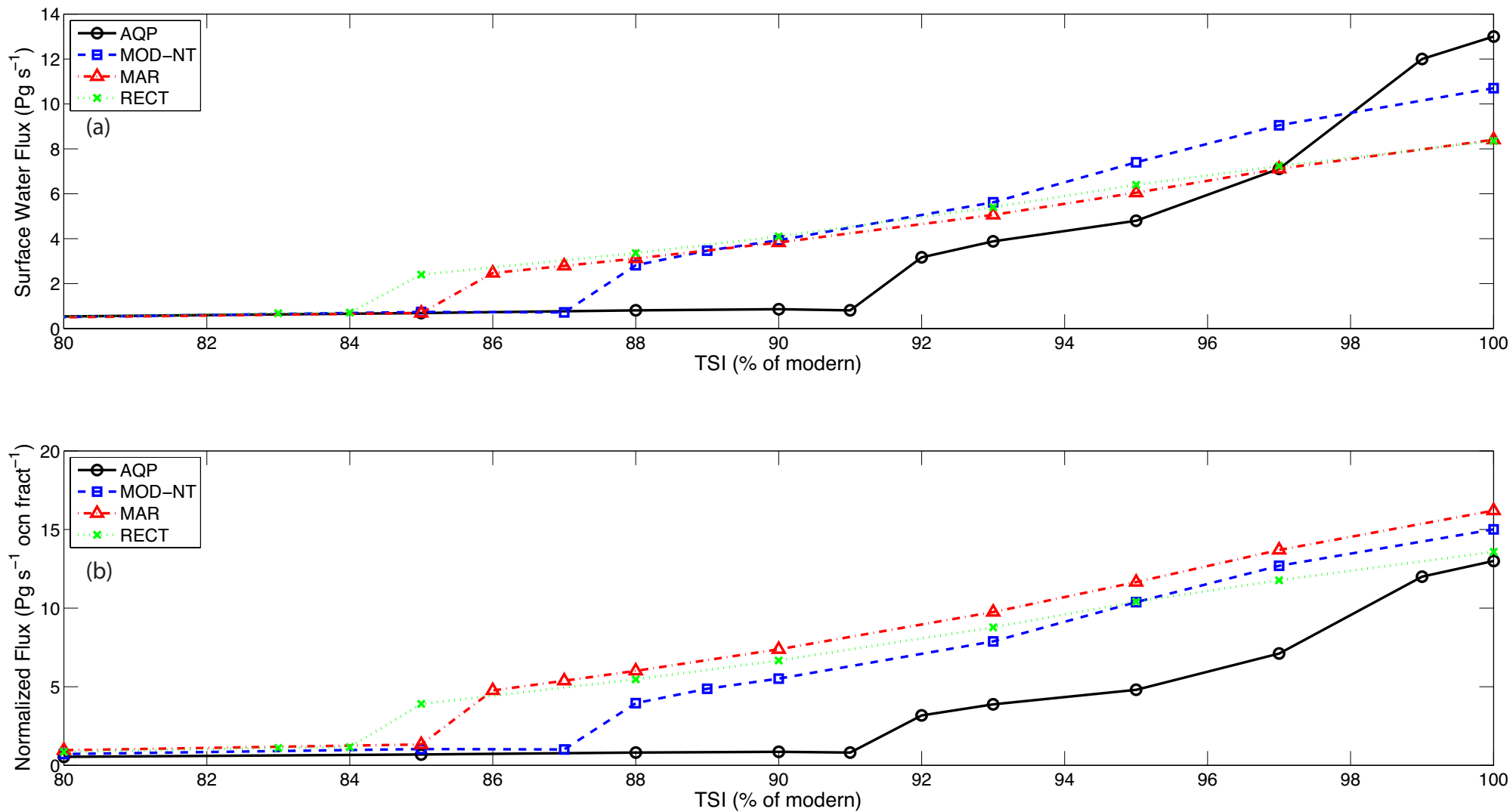
Figure 8. (a) Total surface water flux (Pg s⁻¹) and (b) surface water flux normalized by ocean fraction (Pg s⁻¹ ocean fraction⁻¹) from 30°N/S for all four geographies as a function of TSI. At 100% TSI, surface water flux is highest for the AQP configuration but falls most rapidly with TSI. Surface water flux normalized by ocean fraction shows evaporation in tropical oceans is more efficient for the MAR and RECT configurations than for the AQP configurations.
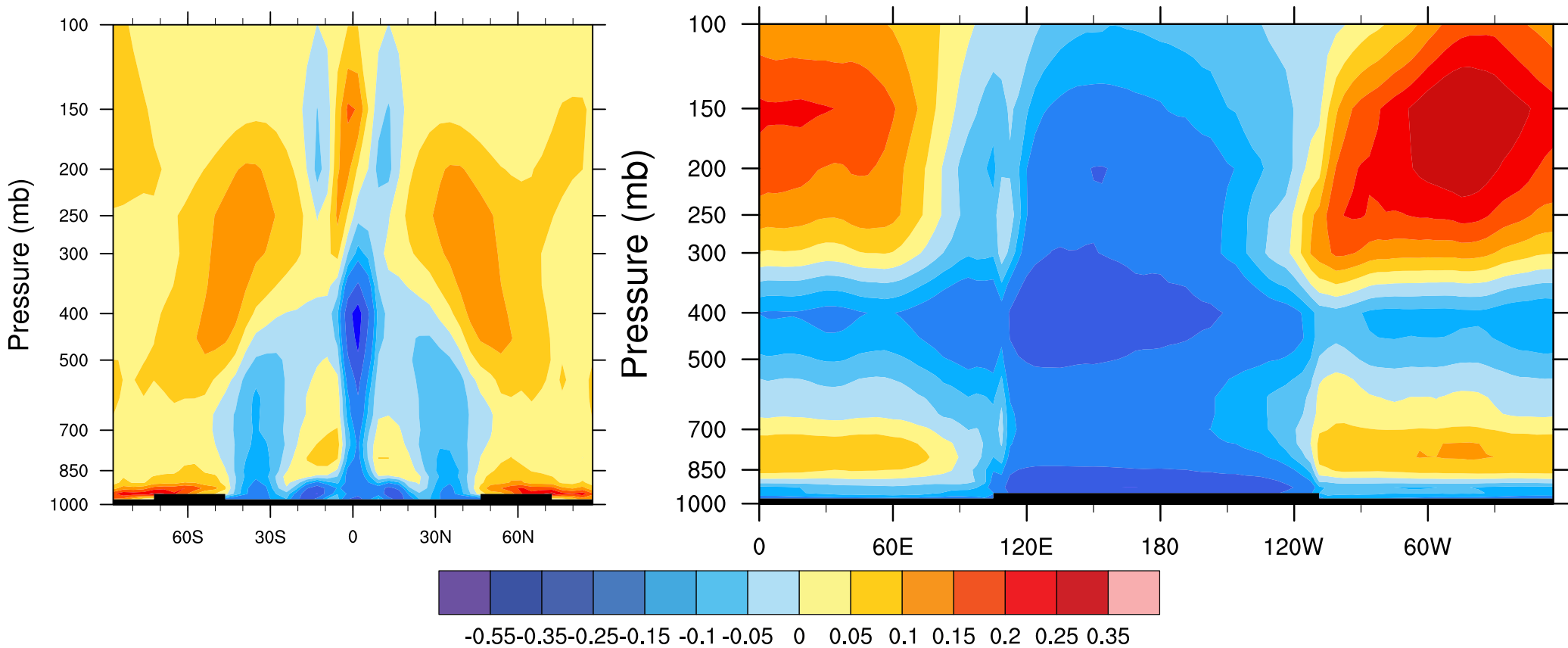
Figure 9. Difference between RECT and AQP vertical cloud fractions at 95% TSI. Both zonally averaged differences (a) and longitudinal differences in the deep tropics (b, 10°N/S) are shown. The Walker circulation simulated decreases the amount of low- and mid-level clouds and increases the amount of high-level clouds, increasing the shortwave cloud forcing in the tropics by 20-40 W m^{-2} while only decreasing the longwave cloud forcing by 10-15 W m^{-2}.
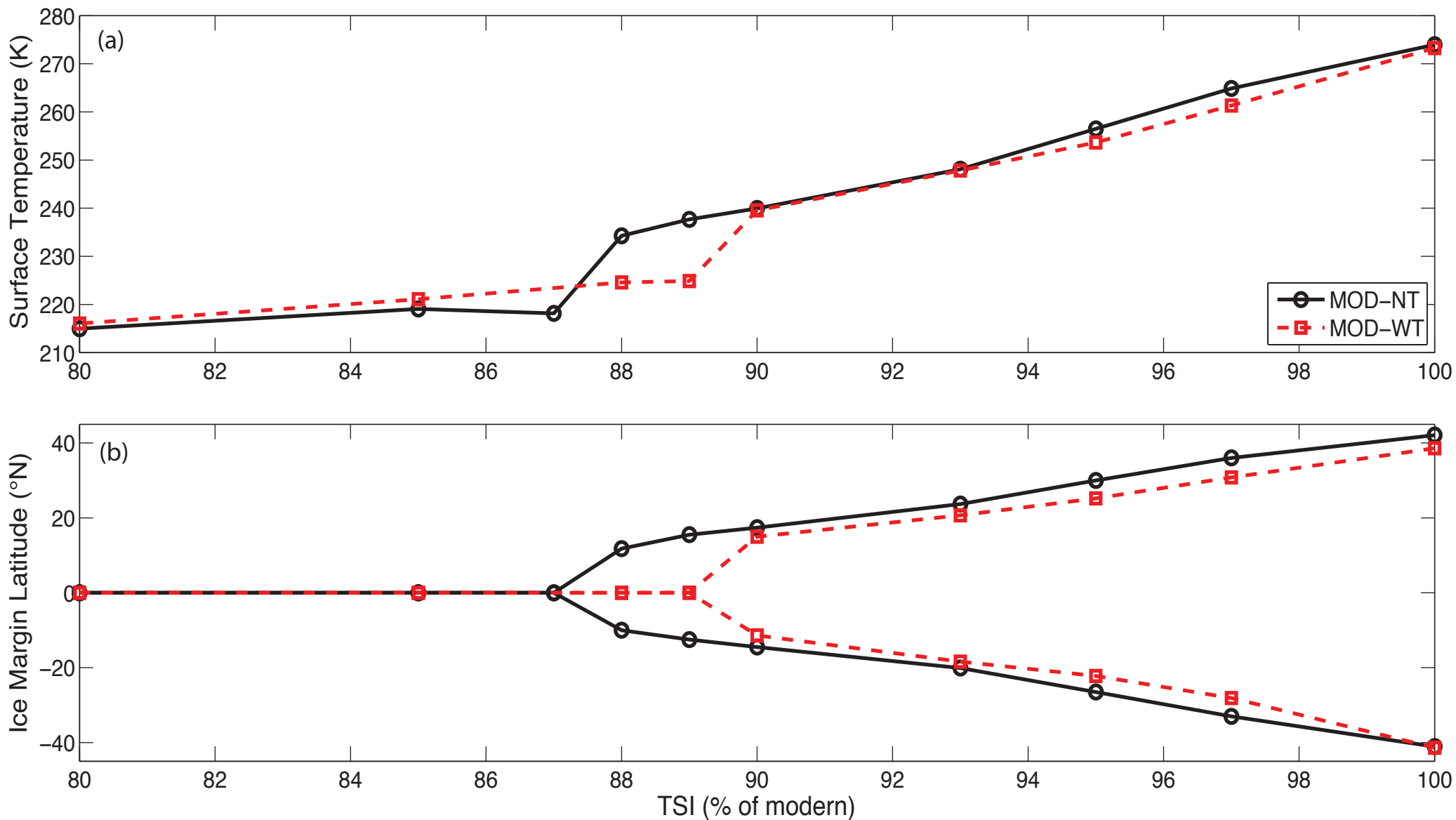
Figure 10. (a) Mean annual surface temperature and (b) ice margin latitude for the MOD-WT and MOD-NT experiments as a function of TSI. Albedos are tightly coupled to temperature and are not shown. Adding topography to the MOD-NT continental configuration raises the snowball bifurcation point from 88% to 90% modern TSI, though above the bifurcation points, little difference exists between global surface temperature and ice margin latitude.
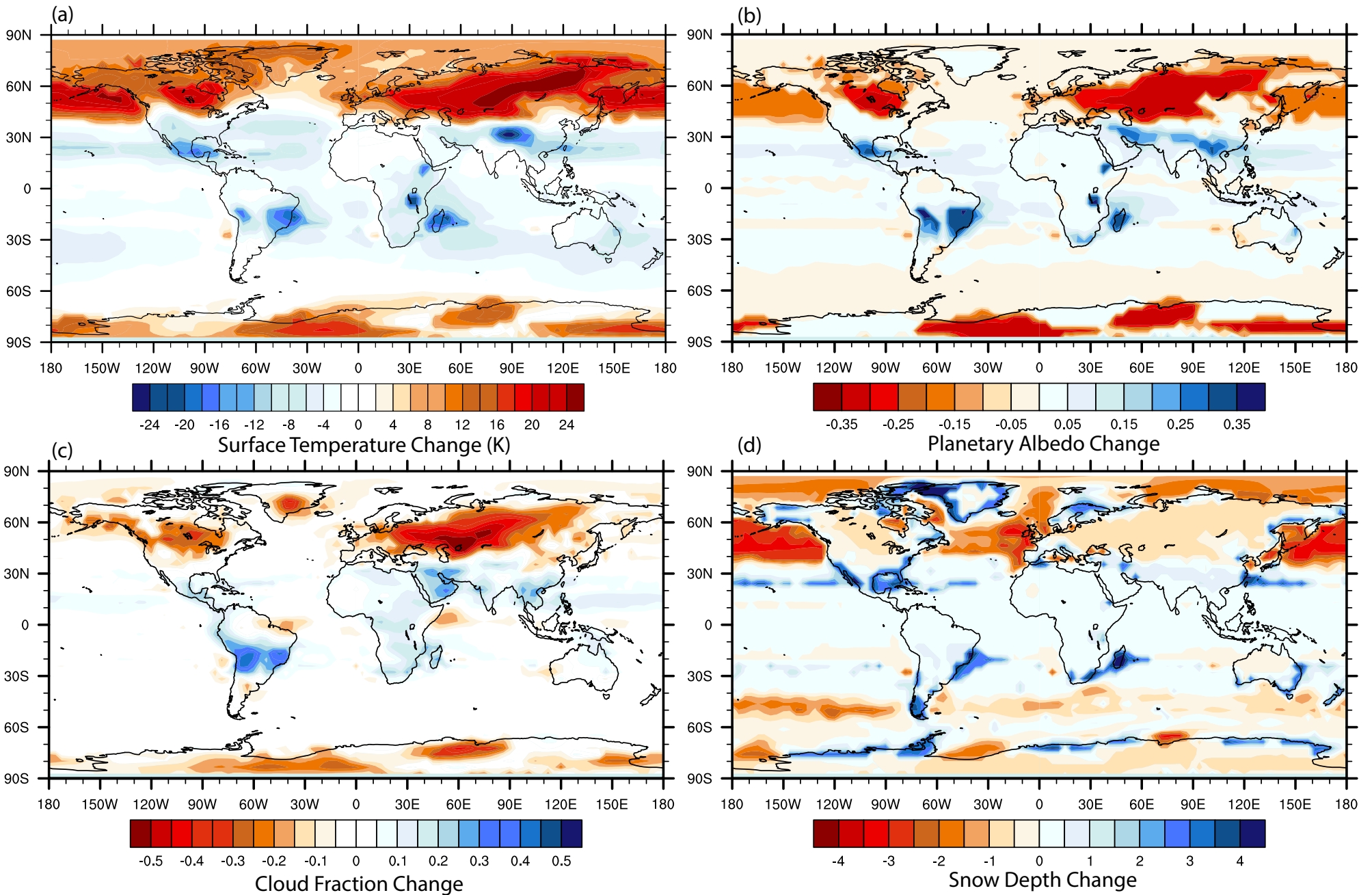
Figure 11. Contour difference plots between MOD-WT and MOD-NT for (a) surface temperature (K), (b) planetary albedo, (c) cloud fraction, and (d) snow depth (meters liquid water equivalent) at 90% TSI. Adding topography reduces the equator-to-pole temperature gradient (a) by raising subtropical albedo and lowering mid-latitude albedo (b), particularly in the Northern Hemisphere where the majority of modern land is located. Albedo changes are driven changes in cloud cover and snow depth (c and d).